Filling in the Gaps: Paleosols as Regional Recorders of Hydroclimatic Change in Northeast China at the Cretaceous – Paleogene

By

Theodore Robert Bobik

B.S., M.S. Temple University, 2019

A Thesis

Submitted in partial fulfillment of the requirements for the Degree of Master of Science in the Department of Earth, Environmental, and Planetary Science at Brown University

PROVIDENCE, RHODE ISLAND

February, 11th 2024

This thesis by Theodore Bobik is accepted in its present form by the Department of Earth, Environmental, and Planetary Sciences as satisfying the thesis requirements for the degree of Master of Science

Date _____ _____

Daniel E. Ibarra, Advisor

Approved by the Graduate Council

Date _____ _____

Thomas A. Lewis, Dean

Acknowledgments

I would like to acknowledge the tireless efforts of many fellow researchers and scientists. Specifically, I would like to recognize Jiquan Chen and Yuan Gao, who continuously provided the necessary samples – as well as challenging and insightful feedback - from across the globe. Thank you Xiaojing Du and Cathy Gagnon for your help in measuring a substantial portion of the traditional carbonate isotopes. Jeremey K. C. Rugenstein, your insight into soil respiration and modeling was essential.

I have also been continually supported by my lab mates at Brown University. Cathy Gagnon, in addition to your help collecting this data, you have been ever present source of support in the lab and have offered incredible instruction on traditional stable isotopic analysis. A big thank you to Natasha Sekhon, my initial guide in the lab. Justin Custado and Sebastian Munoz, thank you both for your encouragement. To Whitney Vieira Ribeiro, Shaw Miller, Jesse Miller, and Jonah Bernstein-Schalet, you are all so talented and incredible undergraduate researchers. Your help in the lab was very appreciated and instrumental. I am excited to see what you all do next.

This work would not have been possible without the aid and guidance of my advisor, Dan Ibarra. Thank you for all of the time and mentorship you have dedicated to my growth as a researcher. As a result, I am a more equipped and confident scientist compared to when I started at Brown University.

I dedicate this thesis to my wife Joanna Mola and our amazing daughter, Shari! Thank you for supporting me through all the years of school and research, and thank you for helping me realize my goals of adding just little more data to the Earth science community.

Table of Contents

List of Tables

List of Figures

1. Introduction

Earth's climate at the termination of the Cretaceous period represents an important analog to Earth's current climate under the influence of anthropogenic climate change i.e., the current warming trend experienced by Earth which ended 50 million years of gradual Cenozoic cooling (Raymo and Ruddiman, 1992; Zachos et al., 2001; Westerhold et al., 2009; Mudelsee et al., 2014). Similarly, during the lead-up to the Cretaceous – Paleogene Boundary (K-Pg), the planet experienced an episode of punctuated warming that truncated the late-Cretaceous cooling trend that began in the Turonian ca. 90 Ma. (Wang et al., 2014; Huber et al., 2018; Tucker et al., 2023). As such, the K-Pg has undergone extensive scrutiny (e.g., Hull et al., 2020; Cox and Keller, 2023) to interpret the hydroclimatic and ecosystem response to abrupt climate change and to strengthen predictions related to future anthropogenic climate change and extinction mechanisms at the K-Pg itself.

The 2023 Intergovernmental Panel on Climate Change predicts a widely heterogeneous climate response with abrupt changes and variance along both zonal and meridional gradients, with significant difficulty in predicting changes in temperature, soil moisture and precipitation on the continents (Fard et al., 2023; Piao and Wang, 2023). Additionally, paleoclimate reconstructions have repeatedly demonstrated the fallibility in assuming that established "status quo" atmospheric dynamics for a given time period will remain unaltered during an episode of climate change (Gasse et al., 2008; Toggwelier, 2009; Kohfeld, 2013; Chen et al., 2019; Abell et al., 2021). Wind speeds, circulation patterns, and the location of convergence zones, i.e.. the Intertropical Convergence Zone (ITZC), have been interpreted to vary in strength, direction, and latitudinal position in

response to global temperature changes in the past. Unfortunately, reconstructing this heterogeneity during the K-Pg is hampered by a paucity of late Cretaceous terrestrial archives and low-resolution data, causing a bias in the existing literature towards the use of primarily marine proxies (Nordt et al., 2003; Wilf et al., 2003; Amiot et al., 2004; Tobin, Wilson, Eiler, and Hartman, 2014; Sprain, Renne, Wilson, and Clemens, 2015). Thus, increasing the understanding of ancient periods of global climate change and the subsequent impact on discrete locations across the planet is paramount for making robust predictions regarding modern anthropogenic climate change and its impact on global population centers.

Fossilized soils, or paleosols, provide a solution to reconstructing the response of a single location to global and regional climate change and offer an avenue to increasing global spatial resolution for a given geologic interval (Mack and James, 1994; Sheldon et al., 2002; 2009; Tabor and Myers, 2015; Caves et al., 2016; Kukla et al., 2022). Soils experience constant exchange with the atmosphere and primarily form as a function of climate. As such, the geochemical and isotopic signals preserved in paleosols can offer insight into drivers of pedogenesis. Numerous studies have demonstrated the utility of soil carbonate stable isotopes (carbon and oxygen) to reconstruct changes in soil temperatures and provide insight into the oxygen isotopic composition of carbonate source waters to infer precipitation oxygen isotope (e.g., Eiler, 2011; Quad et al., 2013; Huntington and Lechler, 2015; Kelson et al., 2018; Ujvari et al., 2019). Further, shifts in soil carbon and the carbon isotopic composition of soil organic matter accurately describe changes in productivity and the evolution of vegetation at the land surface (e.g., Gillsol, et al, 2004; Xie, et al., 2004; Johnson, et al., 2007; Meyers, et al., 2012; Caves et al.,

2016). Additionally, changes in elemental abundance are helpful in reconstructing mean annual precipitation (MAP) and other soil processes related to water balance, soil infiltration and leaching, and climate (e.g., Retallack and Mindszenty, 1994; Retallack and Krull, 1999; Sayyed and Hundekari 2006; Retallack, 1997; Bestland, 2000; Terry, 2001; Sheldon et al., 2002).

Paleosols have already been a significant source of data in the literature reconstructing the hydroclimatic history of the Cretaceous Songliao Basin (Du et al., 2011; Huang et al., 2013; Gao et al., 2015a, Zhang et al., 2018; Gao et al 2021; Chen et al., 2022). Located in the mid-latitudes of Northeast China, the Songliao Basin is one of the largest oil-bearing basins in China, spanning ~2,600 km^2 miles (Fig. 1). The primary period of deposition occurred from the late Jurassic to early Paleogene, with detailed signals of pedogenesis preserved around the K-Pg. Neogene and Quaternary sediments overlay the basin (Wang et al., 2013; 2021). An International Continental Drilling Project started in 2007 to exploit the long basin history with a goal to reconstruct Cretaceous paleoclimate (Wang et al., 2021) The first phase of the project (SK-1n) recovered core sections that contained units deposited across the K-Pg.

Global interpretations of this time period have converged on several themes and drivers of climate change. Latest Cretaceous warming, beginning at ca. 66.4 Ma is largely attributed to Deccan Traps volcanism and the degassing of CO_2 the large igneous province perpetuated for upwards of 800 kyrs (Shoene et al., 2019; Keller et al., 2020; Shoene et al., 2020). The Chicxulub Impact at ca. 66.05 Ma is hypothesized to have many repercussions, with possibly the most consequentially being the effects of fine silicate ejecta circulating in the atmosphere driving a brief cool period (Vellekoop, et al., 2016;

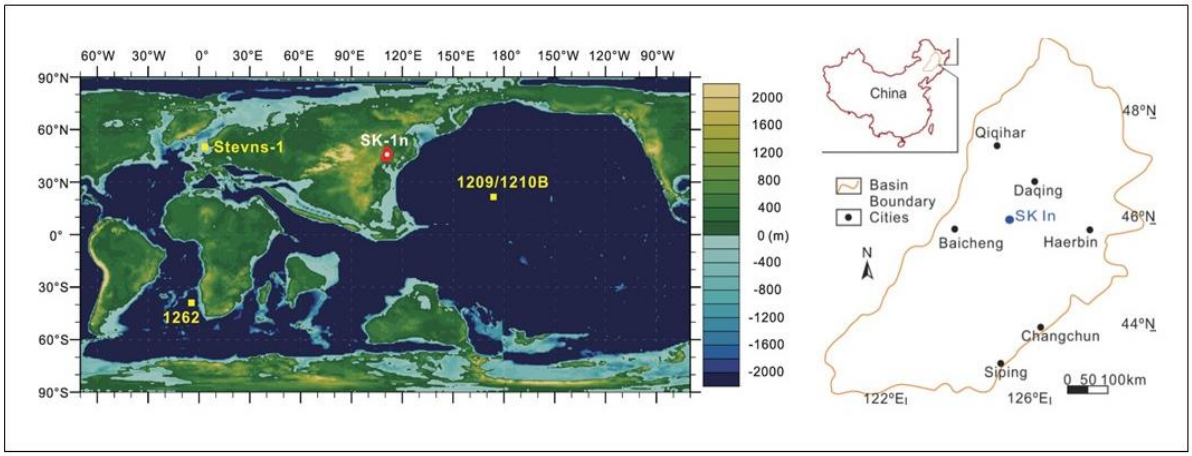

Figure 1. (L) Paleogeography of Songliao Basin (red), and the SK-1n borehole (white), and oceanic drilling project at 70 Ma. Terrestrial colors distinguish paleoelevation (m); (R) SK-1n borehole in context of modern political boundaries. (Modified from Scotese and Wright, 2018; Zhang et al., 2018; Gao et al. 2021)

Senel et al., 2023). Evidence for this so-called "Impact Winter" are contemporaneous declines in oceanic primary productivity. However, declines in marine productivity may be attributed to ocean acidification, as such the effects of the "Impact winter" is ambiguous on terrestrial landscapes (Vellekoop et al., 2014; Henehan et al., 2019).

Here we seek to build on previous work (reviewed most recently by Gao et al., 2021) to interrogate the impact of global events on the hydroclimate response of the Songliao Basin at the K-Pg. By increasing the resolution of the *in situ* soil temperature record, local temperatures can be compared with global and marine signals with respect to the timing and rates of Deccan Trap eruptions. Additionally, we use geochemical soil proxies and stable isotopic record of soil carbonates to reveal regional perturbations in precipitation source and amount recorded in the Songliao Basin in the context of global climate change. Further, using established carbon-isotope-based methods this study also reconstructs terrestrial productivity and soil processes to understand the landscape dynamics and ecosystem productivity of the Songliao Basin at the K-Pg.

2. Sedimentary and Tectonic Background of the Songliao Basin

Sedimentation was first initiated in the upper Jurassic during a period of regional rifting and subsequent lithospheric cooling that allowed for rapid thermal subsidence (Feng et al., 2010; Wang et al., 2015; Zhang et al., 2017). The newly forming basin was filled with a large long-lasting lake that accumulated volcaniclastic and terrigenous sediments (Li et al., 2010; Feng et al., 2013). This period of extensional tectonics is associated with the highest sediment accumulation, occurring over most of the Cretaceous and resulting in 6,000 m of lacustrine, alluvial, and deltaic lithofacies (Wang et al., 2021). In the late Campanian, the basin was influenced by the underlying subducting Pacific plate forcing a period of structural inversion and uplift that increased erosion and caused a westward shift of the depositional center of the basin. Changes in basin morphology explain shallowing paleo-lake levels and long periods of alluvial sedimentation that are preserved as channel/floodplain lithofacies in the Maastrichtian (Du et al., 2011; Gao et al., 2021; Chen et al., 2022). Newly sub-areal lake-margins and floodplains created suitable environments for pedogenesis which are frequently preserved as paleosols across the Mingshui formation (Huang et al., 2013; Gao et al., 2015; 2016; 2021).

The main pedotypes preserved within the formation are Inceptisols, Vertisols, and Alfisols. Near the K-Pg Alfisols are the dominant pedotype (Chen et al., 2022; Gao et al, 2021). Previous studies relied on significant macro- and micro-physical characteristics to determine the presence and type of paleosols (Cheng et al., 2009; Du et al., 2011; Huang et al., 2013; Gao et al., 2016; Zhang et al. 2018; Chen et al, 2022). To distinguish paleosols from lacustrine rocks, free drainage and seasonal wetting and drying was

interpreted from the presence of authigenic carbonate nodules via microscopic analysis, and readily observable slicken sides i.e. macroscopic evidence that clay minerals have undergone shrink-swell from seasonal precipitation (Sheldon and Tabor, 2009). Redox history was interpreted based on color and mottling. Additionally, the presence of downward branch root traces are a clear sign of a subareal environment. Soil classification is based on modern soil analogs described by USDA soil taxonomy. The interpretation of Alfisols at the K-Pg has previously been paired with relative increase in weathering indices to suggest climatic drivers of pedogenesis increase in intensity near the K-Pg (Gao et al., 2015a; 2021; Chen et al., 2022).

3. Principles of Methodology

3.1 Explanation of Isotopic Notation

In order to compare results across laboratories, the isotopic abundance ratio for an element of interest, $^{18}O/^{16}O$ for example, are reported and measured against agreed upon international standards. As such, stable isotope ratios are reported in δ-notation which reports the abundance ratios of isotopes within a given sample as the normalized deviation from a defined isotopic standard following:

$$\delta\ (‰) = (R_{sample}/R_{standard} - 1) \times 1000 \quad (1)$$

In this study, R represents the ratio of either $^{13}C/^{12}C$ or $^{18}O/^{16}O$. Results are reported in per mil (‰) differences, where 1‰ is one-tenth of one percent. δ-notation follows two standard schemes: Vienna Pee Dee Belemnite (VPDB) and Vienne Standard Mean Ocean Water (VSMOW), where samples are reported with respect to an agreed upon ratio of a belemnite (carbonate) or ocean water samples (e.g., Sharp and Wostbrock, 2021).

3.2 Clumped Carbonate Geochemistry and Thermometry

"Clumped isotopes" refers to the phenomena of multiply-substituted isotopologues, where molecules of the same chemical undergo homogenous isotope exchange (Eiler, 2011). These reactions occur when a single chemical, existing in a single phase, reorders the bonding structure of the molecular population to concentrate heavier isotopes, hence *clump*. An example of homogenous isotopic exchange in CO_2 gas follows:

$$^{18}\mathbf{O}^{12}C^{16}O + {}^{16}O^{13}\mathbf{C}^{16}O = {}^{18}\mathbf{O}^{13}\mathbf{C}^{16}O + {}^{16}O^{12}C^{16}O \quad (2)$$

At high temperatures this reordering occurs as the result of a random distribution, referred to as *stochastic distribution* (Gosh et al. 2007; Huntington et al. 2009*)*. Instead, there is a thermodynamic incentive to drive the reaction to the right and concentrate ^{13}C and ^{18}O into a shared bond (Polyakov et al. 2005; Eiler, 2007). The replacement of light isotopes with ^{13}C or ^{18}O will reduce the vibrational frequency and enhance stability, with the doubly substitute bond representing the most favorable configuration (Bigeleisen and Mayer, 1947; Urey, 1947). Heavy isotopes tend to occupy spaces with lower coordination number and higher valence, favoring increased bond stiffness (Young et al., 2015). This propensity of clumping is balanced by the effect temperature has on the system's configurational entropy (Schauble et al., 2006). Higher temperature increases the randomization of the isotope distribution. The cumulative effect of these forces is a temperature-dependent equilibrium constant that increases with decreasing temperature, favoring reactions that promote clumping in a monotonic fashion. Conversely, increasing temperature will drive reactions toward the random stochastic distribution.

The temperature dependence of these reactions creates an opportunity to reconstruct the temperature of the original carbonate precipitation environment by measuring the degree of clumping in CO_2 gas generated from carbonates (Ghosh et al., 2006; Eiler, 2011; Passey et al., 2012). This measurement is generally denoted using the symbol $\Delta_{i,}$ where *i* refers to the mass of a specific heavy isotopologue. For CO_2, the gas derived from calcium carbonate minerals, the specific delta notation is Δ_{47}, the mass of $^{18}O^{13}C^{16}O_,$ and is calculated as follows:

$$\Delta 47 = [\left(\frac{R47}{R47^*} - 1\right) - \left(\frac{R46}{R46} - 1\right) - \left(\frac{R45}{R45^*} - 1\right)] \times 1000 \quad (3)$$

Ri values represent isotopic abundance ratios in ‰ relative to mass 44, i.e., R_{47}, R_{46}, R_{45} are the abundance ratios of 47/44, 46/44, 45/ 44, respectively. With R* values represent a corresponding abundance ratio if the sample contained a stochastic distribution (see Spencer and Kim (2015) which details R* calculation and the necessary assumptions).

The Δ_{47} measurement is the basis for clumped carbonate paleothermometry, a powerful tool that has been applied to many common isotopic reservoirs frequently exploited in paleoclimate studies (Eiler, 2011; Huntington et al., 2010; Henkes et al., 2013; Peters et al., 2013; Quade et al., 2013; Kelson et al., 2020; Huyghe et al., 2022; Huntington et al., 2023). In carbonate minerals, clumping is similar to CO_2 gas, where ^{18}O and ^{13}C reorder into the same carbonate ion group, as follows

$$Ca^{\mathbf{13}}C^{16}O_3 + Ca^{12}C^{\mathbf{18}}O^{16}O_2 = Ca^{\mathbf{13}}C^{\mathbf{18}}O^{16}O_2 + Ca^{12}C^{16}O_3 \quad (4)$$

When measuring the degree of clumping in a carbonate mineral i.e., calcite, a sample is reacted with phosphoric acid (see methods) to produce CO_2. The degree of clumping in the resulting gas reflects the original amount of multiply-substituted carbonate ions composing the mineral.

Δ_{47} values are reported with respect to the carbon dioxide equilibrium scale (I-CDES) and represent "true Δ_{47}" values after calibration to the absolute reference frame (ARF) via an empirical transform function (ETF) derived from a series of linear regressions. The original method for construction and application of the ARF are detailed in Dennis et al. (2011), which measuring several CO_2 gas aliquots of differing bulk composition equilibrated at a range of two to four temperatures. Once equilibrated, the raw Δ_{47} and $\delta47$ are measured for all aliquots and Δ_{47} vs. $\delta47$ is linearly regressed at each temperature. Each regression is projected across the intercept where the Δ_{47} values corresponds to $\delta47 = 0$ i.e., $\delta47$ is normalized to the laboratory's working gas to remove dependence on the bulk isotopic composition. Thus, the Δ_{47} intercept value is characteristic of the formation temperature and used in place of raw values to correct for non-linearity. The Δ_{47}-intercept values for each temperature are together regressed against the "true Δ_{47}" for the given temperature to construct the empirical transform function that project raw samples values into the ARF. Wang et al (2004) details the quantum mechanical and statistical thermodynamic principles used to derive the expected (*true*) values of isotopologues in a thermodynamically equilibrated population of CO_2. As the methods describe in detail below, the carbonate facility at Brown University constructs the ARF measuring only carbonate standards to reduce the uncertainty associated with heated CO_2 gas (e.g. Bernasconi et al., 2018; Bernasconi et al., 2021).

3.3 Soil Respiration and Soil Carbonate $\delta^{13}C$

For studies reconstructing terrestrial environments from paleosols, soil respiration (SR) has become an increasingly valuable proxy for primary productivity (Quade et al., 1989; Quade et al., 2007; Gao et al., 2015a; Caves et al., 2016; Myers et al., 2016; Caves et al., 2018; Licht et al., 2020). Additionally, some studies have demonstrated an empirical relationship between SR and mean annual precipitation (MAP), increasing the potential to evoke SR in hydroclimate reconstructions (Zhou et al., 2009; Da et al., 2021; Da et al., 2023; Zhang et al., 2023). SR is defined as the total flux of CO_2 produced at depth as part of the soil ecosystem and emitted through the soil surface, reported in $gC/m^2/yr$ (Raich and Potter, 1995). The gradient driving the CO_2 flux exists between the relatively high partial pressure of CO_2 that occupies soil pore space, referred to as Soil CO_2 (C_s^*), often 1,000 to 50,000 ppm depending on soil type, and the relatively low pCO_2, typically less than 3,000 ppm (Hönisch et al., 2023), at the soil-air interface that is equilibrated with atmospheric CO_2 (C_0^*). Soil CO_2 is the product of root and microbial respiration (Cerling, 1993). An important distinction when discussing SR is the difference between Soil CO_2 and Soil-respired CO_2. Soil CO_2 is characterized by the following: (1) restriction to soil pore space, (2) representing a concentration in ppmV, and (3) isotopically depleted relative to $\delta^{13}C_{atm}$. Soil-Respired CO_2 refers to overall CO_2 flux, with units of $mmol/m^2/hr$, and is characteristically depleted by at least 4.4‰ relative to soil CO_2. This occurs because the diffusion coefficient of $^{12}CO_2$ is greater than $^{13}CO_2$. Given that the $^{12}CO_2$ and $^{13}CO_2$ species follow their respective gradients through a soil profile, the difference is not exactly 4.4‰ (Cerling, 1999). Empirically, soil-respired

CO_2 is approximately equal to the $\delta^{13}C$ of soil organic matter, which is used as a convenient substitution when modeling SR (Cerling, 1999), an impact we will explore in this work.

The production rate of soil CO_2, at a given depth, is one of the primary influences of the shape of the CO_2 gradient throughout a soil profile, and thus the total flux experienced at the surface. Depth profiles of Soil CO_2 have been extensively described in Cerling (1984), and Cerling (1993), where soil CO_2 diffusion is characterized by the following equation 1:

$$C_s^* = \frac{\varphi^*}{D_s^*}\left(Lz - \frac{z^2}{2}\right) + C_0^* \quad (5)$$

where φ is the constant soil CO_2 production rate (mols/cm^3/s), L is the production depth of CO_2, z is a given soil depth, and D_S^* the soil CO_2 diffusion coefficient. As diffusion occurs towards the soil surface, pCO_2 within the profile decreases under the influence of respiration rate (mmol/m/s), porosity, and the characteristic depth of CO_2 respiration.

SR is modeled from paleosols by measuring the $\delta^{13}C$ of carbonate nodules and exploiting the principle that $\delta^{13}C_{carb}$ reflects isotopic mixing of soil and atmospheric CO_2 (Cerling, 1999). The impact of isotopic mixing has been illustrated by constructing a $\delta^{13}C_{carb}$ gradient throughout a soil profile, where a steep gradient of isotopic enrichment often occurs above 50 cm. While equation 1 describes soil CO_2 diffusion without isotopic distinction, solving for SR from direct measurements of $\delta^{13}C_{carb}$ requires a relationship between the soil CO_2 gradient, φ, and the $\delta^{13}C$ of soil CO_2. This connection relies on the mass dependence of CO_2 diffusion. The rate of diffusion for both soil and atmospheric CO_2 differs with presence or absence of ^{13}C, resulting in molecular weight of either 45 or 44, respectively. Cerling (1984) details how the diffusion coefficients for light and heavy

CO_2 can be substituted into equation 1 along with the $\delta^{13}C$ of soil CO_2, respired CO_2, and atmospheric CO_2. Further, Section 4.7 details how this equation, which was originally constructed as a CO_2 paleobarometer, is exploited to solve for SR (e.g. Gao et al., 2015; Caves et al., 2016; Caves and Chamberlain, 2018).

3.4 Molecular Weathering Ratios and Soil Proxies

The primary method for reconstructing soil forming processes and soil characteristics via bulk geochemistry is to calculate geochemical soil proxies referred to as "Molecular Weathering Ratios" (Hartley and May, 1998; Retallack et al., 2000; Prochnow et al., 2006; Sheldon, 2006b; Hamer et al., 2007). While there are various indices for discrete soil processes, generally, each oxide is divided by its molar mass and used in a ratio between relatively mobile elements, such as alkaline Earth metals, and refractory elements, such as aluminum or titanium (Sheldon and Tabor 2009). The primary interpretative power of these ratios relies on data from B-horizons, where pedogenesis actively occurs (Sheldon et al. 2002). However, Molecular Weathering Ratios are often calculated across an entire soil profile to compare surface and B-horizon values to the C horizon, which largely reflects parent material. Comparing B and C horizon data offer a wholistic view of the degree of pedogenesis and what is obscured by the original overburden provenance (Sheldon, 2006; Stiles and Stensvold, 2008).

This study utilizes (1) the chemical index of weathering (CIW), (2) Al/Si, and (3) Ba/Sr (Table 1). In the following, we describe why that is the case. (1) CIW is an extension of the Chemical Index of Alteration, proposed by Nesbit and Young (1982). However, K is removed from the equation to account for the addition of K through post-

burial metasomatism. CIW is used to interpret the degree of soil formation, where higher values correspond to increased Al, which occurs when parent material weathers to form clays. Likewise, CIW will increase with the depletion of alkali Earth metals, which leach from soils during weathering and clay formation. Additionally, CIW values are used to associate paleosols with potential modern soil analogs and has been empirically demonstrated to correlate to mean annual precipitation (Sheldon et al., 2002). (2) The Al/Si index is an additional measure of "clayeyness" used in tandem with CIW (Sheldon and Tabor, 2009). Combining these two proxies strengthens the ability to discern if the geochemical signals held within a paleosol represent original pedogenic processes. CIW may also reflect unaltered sediment, or leaching that occurred during post-burial processes. In the context of a time series, increased values in an indicator of clay production, like Al/Si that includes variables independent of CIW (i.e. silica) can help verify the interpretation that increases in CIW reflect relatively more soil formation and the presence of more mature soils. (3) Ba/Sr is a measure of leaching and soil drainage, with increased values indicating increased pedogenesis (Thornberg et al., 2019). Sr is much more readily mobile than Ba, which will result in an accumulation and concentration of Ba in B-horizons and a concurrent leaching and removal of Sr. Similar to the relationship between CIW and Al/Si, covariation between all indices would indicate a robust pedogenic signal recorded in the geochemistry.

4. Methods

4.1 Age model

This study targets paleosols identified between 400 – 269 m within the ICDP SK-1n core archived at China University of Geosciences Beijing. These samples are located entirely in the Mingshui formation which was deposited between the late Campanian to the early Danian, spanning the K-Pg (Wan et al., 2013). The age constraints of the Mingshui formation integrate paleomagnetism, biostratigraphy, and palynology with absolute ages derived from $^{206}Pb/^{238}U$ zircon dating extracted from four bentonite beds in the underlying Nenjiang Formation and Qingshankou Formation (Deng et al., 2013, He et al., 2013; Wan et al., 2013; Qu et al., 2014;). $^{206}Pb/^{238}U$ ages are anchored to the Cretaceous Normal Superchron (C34n), 91.4 ± 0.9 Ma to 83.7 ± 0.8 Ma. Extrapolating to the core section targeted in this study, paleosols were formed during C31n-C29r (317.0–530.78 m) with the K-Pg boundary between 342.1 and 317.0 m, in C29r. In addition to the magnetostratigraphy, the placement of the K -Pg is strengthened by an abrupt scarcity of pollen and spores that begin at 360 m and continue to 263.4m which has been associated with global palynofloral changes that occurred at the boundary (Li et al, 2011).

This study uses the astronomical time scale established by Wu et al. (2014). The ATS model is based on the power spectra, Fourier transformation, and wavelet analysis of Thorium (Th) well log data. Periods of Th accumulation in mudstone, and depletion in sandstones, are treated as a paleoclimate proxy that suggests increased weathering during warm episodes, enabling Th-based cyclostratigraphy. Cycle wavelength ratios in the Cretaceous section of the SK-1n core approximate to 20:5:2:1 and are interpreted as 405 kyr and 100 kyr eccentricity, 38.4 obliquity, and 20 kyr precession, respectively. Due to limitations of age models for the Mesozoic, Th cycles are only tuned to the target curve of 405 kyr eccentricity band. In the Mingshui, the ATS is anchored at 342.1 m by the

boundary C29r/C30n boundary age, 66.3 Ma. The resulting K-Pg boundary is placed within 317 and 329 m, with the ATS demarcated K-Pg at 318 m.

4.2 Paleosol identification and Sample selection

Both matrix and nodule samples were selected for elemental and isotope analysis. New samples were targeted based on their proximity to the K-Pg and selected at the highest resolution possible, averaging 19 kyr with a modal age difference of 10 kyr across the sample set. Where available, time equivalent samples were selected from the same soil horizon for comparison. Where the delineation of the paleolandscape remained ambiguous, depth to carbonate nodules was estimated from the average depth of contemporaneous nodules found in the composite SK-1n core, which ranged between 30 to 50 cm (Huang et al., 2013; Gao et al., 2015a). The carbonate concentration of all samples were all previously estimated based on sample weight and the voltage produced by traditional stable isotope measurements (Gao et al., 2015; 2021; *This Study*). All sample were dried and ground to a fine powder via mortar and pestle prior to elemental and isotopic analysis.

4.3 Traditional carbonate stable isotope measurements

In advance of targeting samples for clumped carbonate measurements, 81 nodule and matrix samples were analyzed for new traditional $\delta^{18}O$ and $\delta^{13}C$ measurements as a larger preliminary data set. Measurements were made using a Thermo Scientific™ 253 Plus 10 kV Isotope-Ratio Mass Spectrometer with a Kiel IV carbonate peripheral at Brown University. Sample aliquots were weighed out to ensure ~50 μg of carbonate

within the total aliquot to achieve the desired measurement voltage (3-6 V) and reacted with phosphoric acid at 70 °C (e.g., Gagnon et al. 2023). External precision of oxygen and carbonate was based upon repeated measurements of two internal laboratory standards, BYM63150 and Carrara 63150, calibrated against NBS 18, NB19, IAEA 603, ETH2 and ETH4.

$\delta^{18}O$ and $\delta^{13}C$ are both reported with respect to the Vienne Peedee Belemnite scale. $\delta^{18}O$ is also converted to the Vienne standard mean ocean water scale using the IUPAC recommended transform function:

$$\delta^{18}O_{vsmow} = \delta^{18}O_{vpdb} \times 1.03092 + 30.92‰ \quad (6)$$

4.4 Clumped Carbonate Isotopic Analysis

Clumped isotopic analyses were also conducted at Brown University on the same mass spectrometer using a different peripheral. Samples were weighed into silver vials with the target weight of the total sample calculated such that between 6 – 7 mg of carbonate would be present in the overall sediment to achieve 16 V when measuring mass 44 CO_2. The long running S.D. of external standards for both $\delta^{18}O$ and $\delta^{13}C$ is < 0.1 ‰. Carbonate was converted to CO_2 gas using an automated carbonate extraction line referred to as the IBEX (Isotope Batch EXtraction system), a peripheral manufactured by Protium^{ms} (John and Davis, 2015; Davies, et al., 2021). Matrix and nodule samples were reacted in a common acid bath at 90 °C for ten minutes at ~90 °C and frozen into the first of two purification traps at -197 °C, removing water and other non-condensable gasses. The trap was subsequently heated to release only sample CO_2 and He carrier gas transported the sample across a silver wool sulfur trap and Porapak filled GC column for further purification and removal of organic matter. The sample was frozen into a second

trap before being released and concentrated in an external microvolume before analysis. Clean sample gas is then thawed from the microvolume into the sample-side bellows of the same Thermo Scientific™ 253 Plus 10 kV Isotope-Ratio Mass Spectrometer (IRMS) used for traditional measurements described above. Measurements at Brown University are made following procedures outlined in Eiler and Schauble (2004), Huntington et al. (2009), Dennis et al. (2011), Adlan et al., (2020), and Davies, et al., (2021).

At Brown University, Δ_{47} data $_{is}$ projected in ARF space by measuring the internationally calibrated carbonate standards: ETH 1 ETH 2, and ETH 3, in lieu of CO_2 gas, as suggested by Bernasconi et al. (2021). The non-linearity correction was based on Δ_{47}-intercept values derived from projecting a linear regression between the average raw Δ_{47} vs. $\delta 47$ values for ETH 1 and ETH 2. Collectively, the Δ_{47} intercept values for all three standards are regressed against their most recently accepted values, as reported in Bernasconi (2021), resulting in a unique ETF for each session (typically 1 to 3 weeks in duration). Data reduction was streamlined by uploading raw data into the Easotope Software developed by John and Bowen (2016). All calculations are made using the ^{17}O corrections as outlined in Brand et al. (2010). Clumped carbonate values are background corrected using a mass 47.5 cup as described in Fiebig et al. (2019) with mass scans occurring before and after each carousel of samples (typically 1 to 3 days).

4.5 Δ_{47} Temperature Reconstruction

Temperature is estimated using eq. 3, the calibration presented by Anderson et al. (2021).

$$\Delta_{47}CDES = \frac{0.0391\times10^{6}}{T^{2}} + 0.154 \quad (7)$$

Here, $\Delta_{47}CDES$ represents the ARF value for each sample used to solve for temperature, T, in Kelvin. This calibration is the work of a multi-lab collaboration highlighting the difficulty of modeling temperatures at Earth surface conditions and the discrepancies that persist across laboratories. Eq. 3 is derived from a multi-study composite calibration based in carbonate standardization, as opposed to heated gas, which is broadly applicable to different geologic materials and emphasizes measuring standards that reflect colder temperatures relevant to terrestrial paleoclimate reconstruction (e.g., Peral et al., 2018; Breitenbach et al., 2018; Jautzy et al., 2020; Meinicke et al., 2020; Anderson et al., 2021), highly relevant to this work.

4.6 Reconstructing porewater $\delta^{18}O$

The $\delta^{18}O$ of soil carbonate is a product of the $\delta^{18}O$ of the soil porewater it precipitates from and the environmental temperature i.e., soil temperature, which controls the isotopic fraction factor between porewater and calcite. Porewater $\delta^{18}O$ is calculated following Kim and O'Neil (1997), solving for α:

$$1000ln\alpha(\text{Calcite} - \text{H}_2\text{O}) = 18.03(10^3\text{T}^{-1}) - 32.42 \quad (8)$$

Where T is Δ_{47} derived temperature, and α is the fractionation factor between calcite and porewater $\delta^{18}O$. Once α is defined for a given temperature, $\delta^{18}O_{pw}$ is calculated as:

$$\delta^{18}\text{O}_{\text{pw}} = ((1000 + \delta^{18}\text{O}_{\text{pw}})\,/\alpha) - 1000 \quad (9)$$

The kernel estimated Δ_{47}-temperatures from this study were linearly interpolated to the ages associated with $\delta^{18}O_{carb}$ measurements that do not have carbonate clumped isotope measurements in Gao et al (2015a; 2021) and Huang et al, (2013) to recalculate and improve the composite porewater record that has previously relied on sea surface

temperature values from marine deposits (Linnert et al., 2014). Kernel smoothing methods based on methods in Gao et al. (2015a) and Caves et al. (2016).

4.7 Modeling Soil Respiration

Soil respiration is modeled following methods outlined in Caves et al. (2016) and Gao et al. (2015a), in which the CO_2 palebarometer described in Cerling (1984, 1993, 1999) is inverted to solve for SR:

$$SR = L\left[\frac{D_s C_{atm}(\delta_{atm}-\delta_s)}{(Lz-z^2 2^{-1})(\delta_s-1.0044\delta_\theta-4.4)}\right]\frac{1}{\varepsilon} \quad (10)$$

Here, z is depth-to-carbonate in the soil profile, L is the production depth of CO_2, C_{atm} is the atmospheric concentration of CO_2 in ppm, Ds is the diffusion coefficient for CO_2 in soil (cm2 /s), and ε is soil porosity. The delta notation represent the $\delta^{13}C$ of the atmosphere (atm), soil CO_2 (s), and organic matter (θ). Inputs into the equation represent a combination of constant, assumed, and calculated values. The actual value for z is estimated by correcting for burial compaction via the "decompaction" transfer function (Sheldon and Retallack, 2001; Huang et al. 2013; Gao et al., 2015a; 2021). C_{atm} is calculated using data from the multi-proxy, multi-research group, collaborative project, "Paleo-CO_2", which integrates boron, leaf gas exchange, liverworts, Nahcolite, paleosol carbonate, phytoplankton, and stomatal frequency proxies (Hoenisch, 2021). To account for error, a randomizer was applied to each mean pCO_2 value to add within +/- 1σ (reported from original study) over 500 iterations. Epanechnikov kernel-smoothing was then applied to the iterated dataset at a .40 Ma bandwidth. For the final SR calculation,

the kernel estimated record was linearly interpolated to the ages of paleosol carbonate in this study and converted from ppm to mmol using code from Caves et al. (2016) using our carbonate Δ_{47}-temperatures. δs derived using the $\delta^{13}C$ measured from paleosol carbonate, and Δ_{47}-temperatures to solve for the fractionation factor and calculate δs:

$$1000ln\alpha(\text{Calcite} - \text{CO2}) = 11.709 - 0.116(\text{T}) - 2.16\text{x}10^{-4}(\text{T}^2) \quad (11)$$

δθ is an assumed value of -25 ± 1‰ , based on soil organic matter in the upper most section of the underlying Nenjian Formation (Song et al., 2013). δ_{atm} is assumed to be a constant -5‰, reflecting late Cretaceous estimations (Tipple et al. 2010). This value lacks uncertainty, so we do not assign a value. The kernel estimated Δ_{47}-temperature and pCO_2 produced records by this study were linearly interpolated to the ages of $\delta^{13}C_{carb}$ measurements in Gao et al (2015a) and Huang et al, (2013) to recalculate and improve the composite SR record. SR values exceeding 3,000 $gC/m^2/yr$ are considered outliers and discarded based comparison with comprehensive global SR records spanning 1961 – 2007 (Bond-Lamberty and Thomson, 2010)

4.8 Major Elemental Analysis

The bulk geochemistry of paleosol matrix was analyzed in the Environmental Geochemistry Lab at Brown for major and trace elements following procedures developed at Boston University and outlined in Murray, Miller, and Kryc, ODP Technical Note 29(2000). 0.16 g of lithium metaborate was weighed into graphite crucibles as an evenly distributed mound containing a small indentation where sample was subsequently deposited. 0.040 (± 0.005) g of finely ground sample was weighed and carefully added into the flux and gently homogenized. Three additional crucibles

including only the lithium metaborate flux were processed and measured as blanks. The mixture was heated at 1100 ℃ for 10 minutes, or until fully melted, and added to a 10% HNO_3 solution. The solution remained on a shaker table for 24 hours to allow for complete dissolution. A 20 ml aliquot was removed via syringe and filtered using a 0.45um filter to remove graphite. To ensure accurate quantification and calibration, the following six USGS and NIST certified reference materials were fused and digested in the same manner as samples: Montana Soil 2711, MAG-1, BIR-1, BHVO-2, 2702, 1646a (Jochum et al., 2012).

All aliquots were analyzed using a Thermo Scientific iCAP 7000 Series Inductively Coupled Plasma Optical Emission Spectrometer (ICP-OES). An additional aliquot comprising a composite of all samples, standards, and blanks was measured at a frequency of once per ten samples to assess any systematic drift over the course of the run. Primary elements of interest were Al, Si, Ca, Na, Mg, and P. Raw data was corrected for drift and a dilution factor was applied to each sample before quantification. CaO values are corrected to CaO* following McLennan (1993). CaO derived from apatite is corrected to CaO' via

$$CaO' = CaO\text{-}P2O5 \times 10/3 \quad (12)$$

If the correct CaO' value is less than Na_2O, CaO' is used as CaO*. When CaO' exceeds Na_2O, Na_2O is substituted for CaO*. Results are reported as either percent oxide by weight, or parts per million (ppm). CIW as described in section 3.4 is calculated as follows:

$$CIW = 100 \times \frac{Al}{Al+Ca+Na} \quad (13)$$

where elementals represent molecular weathering ratios reported in weight percentages. CIW is also used to calculate mean annual precipitation via the climofunction function presented by Sheldon et al. (2002):

$$\mathrm{MAP} = 221.12e^{0.0197\mathrm{CIW}} \quad (14)$$

Equation 14 is additionally applied to geochemical results published in Gao et al. (2021).

5. Results

5.1 Carbonate and Porewater $\delta^{18}O$ and $\delta^{13}C$

The mean $\delta^{18}O$ and $\delta^{13}C$ across the data set are 21.20‰ (VSMOW) and -8.03‰ (VPDB), respectively. 66.05 Mya demarcates the boundary between two distinct isotopic populations, where late Cretaceous oxygen values (~20‰) reflect a more depleted signal, and carbon values (~-7.5‰) appear more enriched with respect to carbonated formed after 66.05 Mya (Fig 2.). Early Danian samples have an average $\delta^{18}O$ ~22‰ and a $\delta^{13}C$ of ~-9‰. Results in this study agree with overall trends and stable isotopic ratios reported in previous studies where applicable, replicating a ca. 2 ‰ excursion in both $\delta^{18}O$ and $\delta^{13}C$ at 66 Mya (Gao et al., 2015a; 2021; Zhang et al., 2018).

Matrix samples show agreement with values derived from near contemporaneous nodules in both carbon and oxygen. Results largely derived from matrix samples express a previously unidentified excursion between 66.24 – 66.09 Mya, where a positive ~1.5 ‰ shift in $\delta^{13}C$ is coincident with a negative shift in $\delta^{18}O$ of similar magnitude. Following the termination of this excursion there is an immediate 2‰ rebound in $\delta^{18}O$ and a similar but lagging rebound in $\delta^{13}C$. Following the excursion beginning at 66.0 Mya, identified

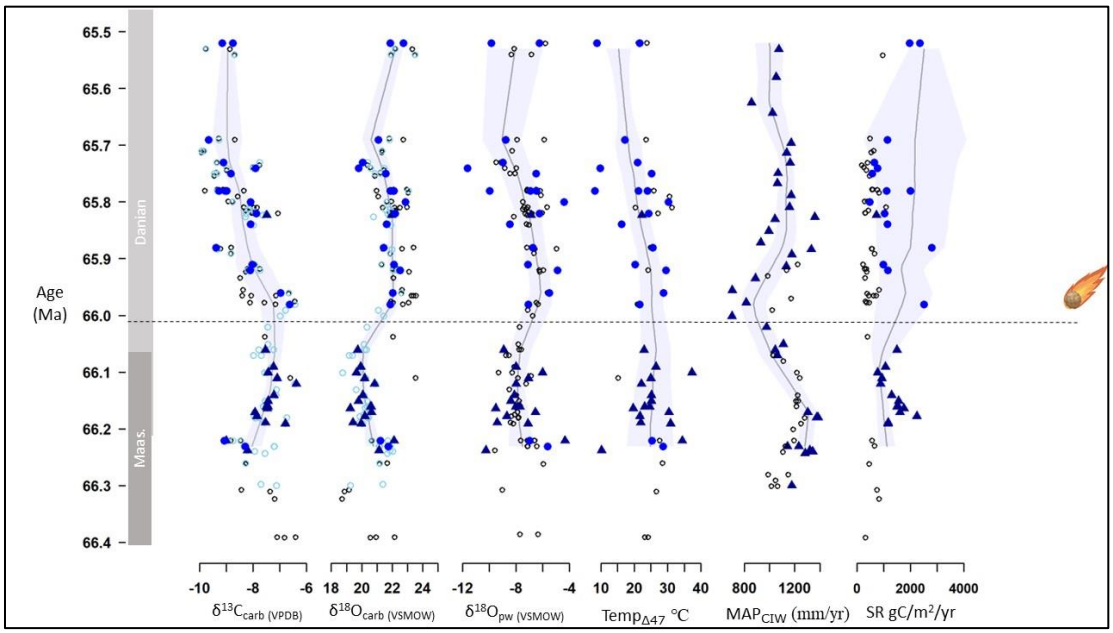

Figure 2. Stable isotopic results with MAP and SR, Clumped carbonate data set: dark blue triangles = matrix, dark dots = nodules; Traditional isotopic dataset: light blue circles = traditional isotopic results (new Kiel data); clear circles= previously published data (Huang et al., 2013; Gao et al., 2015; Zhang et al., 2018). Kernal smoothing only represents new results produced in this study (full data kernel smoothing in section 6.1)

by Gao et al. (2015a), a slight positive shift in $\delta^{18}O$ occurs between 66.7 – 66.5 Mya, without any signs of covariance in $\delta^{13}C$.

Mean value for the calculated porewater $\delta^{18}O$ is -7.50 ‰, with a late Cretaceous mean value of -7.59‰ (VSMOW) and Danian mean value of -7.40‰. While the overall dataset is largely stable, Danian porewater values include a period of substantial spread, as much as 4‰ , in near contemporaneous samples formed at approximately 65.75. Additionally, carbonates formed in the early Danian are the only samples that experience a sustained shift in $\delta^{18}O$pw. Between 66.0 – 65.75 Mya, values remained enriched by 2-3‰ relative to the late Cretaceous and later Danian carbonates.

5.2 Δ_{47} Temperature

Δ_{47}-derived temperatures produced in this study range between 8.76 and 37.56 ℃ with an average standard error on replicate measurements of 2.4 ℃. As in $\delta^{18}O$ and $\delta^{13}C$, two distinct features are delineated by the K-Pg: (1) Elevated temperatures in the late Cretaceous, and (2) an overall cooling trend in the early Paleogene. Late Cretaceous temperatures include the hottest temperatures, with 4 samples indicating a soil temperature above 30 ℃ , and a maximum soil temperature of 37 ℃ at 66.05 Mya. However, the majority of late Cretaceous samples are clustered near the kernel smoothed mean of 25 ℃ and the second coldest temperature, 10.20℃ is measured at 66.237 Mya. Danian temperatures comprise an overall cooling trend, with the kernel smoothed temperature trend indicating ca. 10 ℃ of steady cooling throughout the early Danian. Included during the period of overall cooling are several discrete elevated soil temperatures approximately between 65.90 – 65.80 Mya.

5.3 Soil respiration

SR flux values modeled in this study are higher than in previous studies. Late Cretaceous values average 1349.9 g C/m^2/yr. The range for this period is 764.9 – 2,236.5 g C/m2/yr. Maximum values, in excess of 1,000 g C/m2/yr fall between 66.24 – 66.18 Mya. Following 66.0 Mya, SR increases overtime. The average for Danian SR is 1,316.6 g C/m2/yr. The range for this period is 468.1 – 2,803.3 g C/m^2/yr with a higher frequency of SR rates > 1000 g C/m^2/yr. The early Danian is largely stable with a potential increasing trend beginning at 65.7 Mya., terminating with two time equivalent nodules representing 1093.5 and 2,346.4 g C/m^2/yr, one of the highest values in the

study. Calculated SR values and the relative impact of model inputs (e.g. temperature, δ13Corg) are further interrogated in section 6.4.

5.4 Elemental Analysis and MAP

Late Cretaceous values of CIW, Al/Si, and Ba/Sr are all elevated compared to the early Paleogene (Fig 3). However, the maximum CIW, 94, occurs at 65.32. Prior to the impact, maximum CIW(93) and Al/Si (0.49) occur at approximately 66.18 and 66.25 Ma, respectively. Late Cretaceous Ba/Sr is notably excessive for soils, with maximum Ba/Sr (24) occurring at approximately 66.02 Mya, with a likely outlier (51.15) occurring at 66.27 Mya. All indices show a sharp decline across the K-Pg. CIW reaches minimum values between 60 -70 near 60 Mya before increasing to ca. 80 at 65.9 Mya, where samples are sustained with low variance across the remainder of Danian aged samples. Unlike CIW, Al/Si and Ba/Sr do not show any sustained
recovery after 66.0 Mya. Al/Si values converge at ca. 0.2, with two outliers between 65.9 – 65.8 Mya that impact the overall kernel smoothed average. Similarly, Ba/Sr values remained under 2.5 with the exception of two outliers (12.87 and 9.80) that are coincident with outliers in Al/Si.

Mean annual precipitation calculated using equation 14 ranges from 699 to 1,385 mm/yr. Initially, MAP increase from 1,176 to 1,385 mm/yr from 66.30 to 66.18 Ma followed by a steady decline to 699 at 66.00 Ma. MAP rebound with a steady increase to

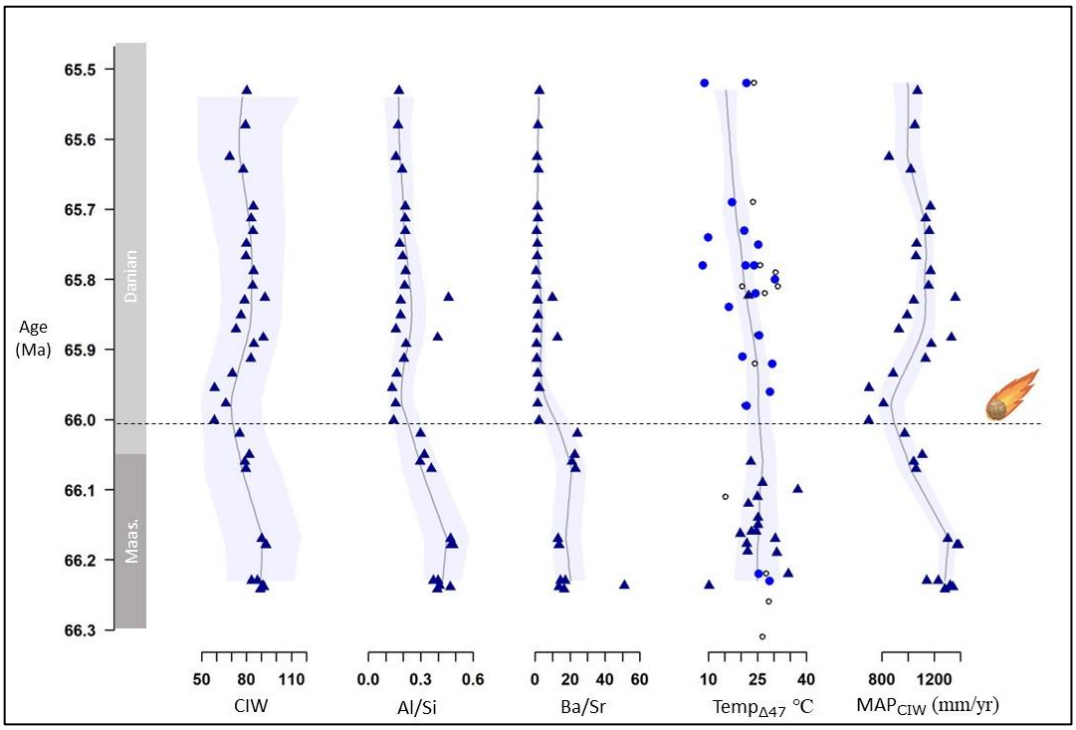

Figure 3. Molecular weathering rations with relevant climate data. Asteroid denotes timing of Chicxulub impact 66.05 ± 0.031 Ma (Previous Page)

1,332 mm/yr at 65.81, where MAP remains near 1,000 mm/yr for the remained of the dataset.

6. Discussion

6.1.1 Hydroclimate changes across the K-Pg

Our additional measurements on the Songliao Basin paleosols clarify the regional hydroclimate dynamics with increased and significant updates to the temperature record that now enable a more meaningful correlation to global terrestrial records. The increased resolution gained by the exploitation of soil matrix samples has rectified a persistent gap in the record between 66.23-66.1 Ma from previous studies (Huang et al., 2013; Gao et al., 2015a; Zhang et al., 2018; Gao et al., 2021). The resulting comprehensive soil

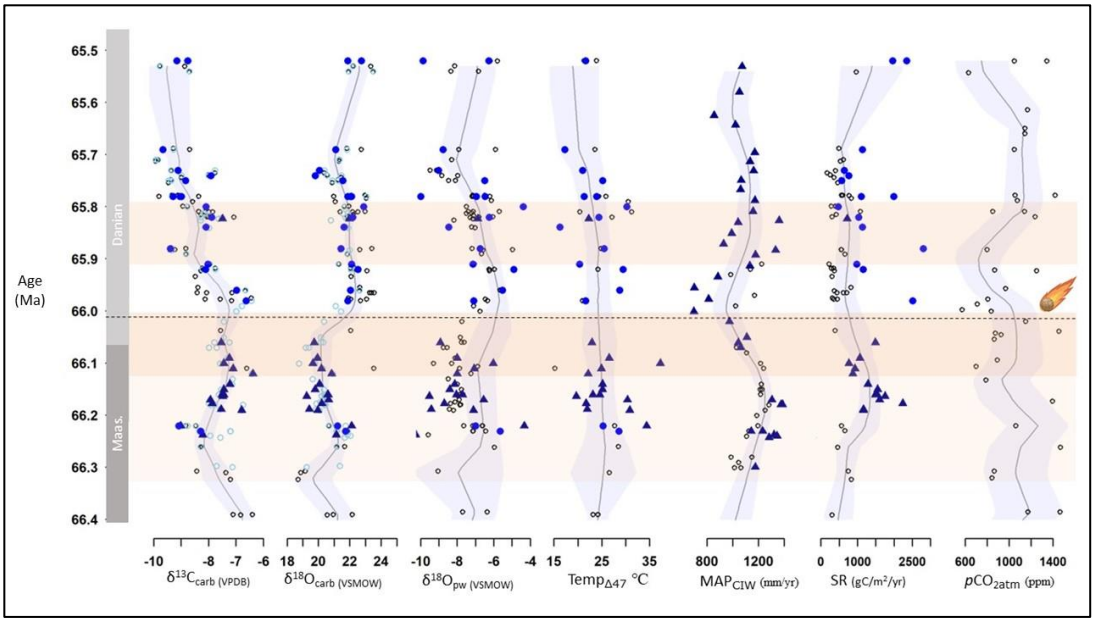

Figure 4. Updated results to include supplementary data in Kernel smoothing. $pCO2_{atm}$ values derived from the paleoCO2 project (Hönisch, 2021) Color bars represent timing of main phase deccan traps eruptions as interpreted by Schoene et al. (2019), darker colors denote more vigorous eruption rates; Asteroid denotes timing of Chicxulub impact 66.05 ± 0.031 Ma

temperature record better elucidates the two-step warming progression at the K-Pg. Step one occurs at 66.40 Ma after nearly one million years of < 20 ℃ conditions with an abrupt increase where temperatures are largely sustained between 25 and 28 ℃ until ~66.00 Ma (Fig 4). This is significant as it aligns with the onset of Deccan Traps volcanism (Sprain et al., 2019; Scheone et al., 2019) and has implications for global temperatures as it confirms the region experienced warming during the Late Maastrichtian Warming Event (LMWE), discussed further below (Sections 6.1.2 and 6.2.1). The second step occurs within this overall warming period, between 66.22 and 66.17 Ma, delineated by a cluster of discrete temperatures > 30℃. There is no significant abrupt cooling directly pre- or post- Chicxulub impact. Instead, our updated temperature record suggests a gradual cooling begins at 66.00 Mya. With these results we recontextualize a group of previously measured discrete temperatures at ~65.8 Ma that

return to > 30 ℃, also replicated in our study (cf. Zhang et al., 2018). We interpret this as an ephemeral temperature excursion overprinted on the overall cooling trend that is also likely linked to the pacing of post K-Pg Deccan Traps activity (discussed below in section 6.2.1). Lastly, we conclude the singular abrupt cold interval at 66.11 Mya (15℃) measured by Zhang et al. (2018) in one sample is likely an artifact. The data in aggregate clearly show both the temperature and the $\delta^{18}O_{carb}$ of that sample are outliers and should be disregarded.

The pairing of our $\delta^{18}O_{pw}$ and MAP reconstructions has also elucidated the hydrological signal embedded in both the $\delta^{13}C_{carb}$ and $\delta^{18}O_{carb}$ trends. We conclude that trends in $\delta^{18}O_{carb}$ almost entirely reflect changes in the isotopic composition of porewater with little contribution

from major changes in temperature. Trends in $\delta^{13}C_{carb}$ in paleosols are dominated by changes in MAP and relative aridity (Retallack, 2005; Kohn, 2010; Montañez, 2013). We suggest this insight is potentially helpful in interpreting parts of the Songliao record with limited temperature and porewater measurements. We base our assessment of $\delta^{18}O_{carb}$ on two lines of evidence: (1) changes in $\delta^{18}O_{carb}$ are not explained by the 0.35‰/℃ temperature sensitivity of oxygen isotopes related to oxygen fractionation between water and carbonate (e.g., Chamberlain et al., 2012) and (2) more generally, there is no apparent correlation between formation temperature and $\delta^{18}O_{carb}$. We find shifts in the total $\delta^{18}O_{pw}$ record are on the order of modern oscillations between seasonal precipitation source (~3‰; Araguás-Araguás et al., 1998; Li et al., 2012), however the overall $\delta^{18}O_{pw}$ record falls within the range values previously interpreted as primarily monsoonal derived precipitation (Gao et al. 2015a; 2021; Zhang et al., 2018; Chen et al., 2022). We

discuss issues with this correlation to modern analogs and obscuring factors, such as evaporative enrichment below (see section 6.3). Trends in $\delta^{13}C_{carb}$ almost entirely follow MAP indicated by shared inflection points at 66.20 and 65.98 Mya, with $\delta^{13}C_{carb}$ enrichment consistently occurring during decreasing MAP. While this often results as water stress decreases the efficiently of plant ability to discriminate between heavy and light carbon isotopes, $\delta^{13}C_{carb}$ is also a reflect of pCO_{2atm} (Tipple and Pagani, 2007; Kohn 2010; Montañez, 2013; Caves et al., 2016). We find it notable that during this period increased pCO_{2atm} there is no apparent correlation with $\delta^{13}C_{carb}$ ($r^2 = 0.14$), and may be an important consideration when modeling SR or in any future use of the soil carbonate CO_2 paleobarometer (e.g., Honisch et al., 2023).

More broadly, temperature, isotopic, and MAP trends in the Songliao Basin illustrate a hydroclimatic history defined by two distinct periods: (1) elevated temperatures and relatively elevated MAP occurring in the latest Cretaceous contemporaneous with the Late Maastrichtian Warming Event, and (2) sustained long-term cooling in the early Paleogene that include discrete spikes in temperature, and evidence for short-lived changes in precipitation source to the basin. Coherent with these results, trends in soil processes strengthen the interpretation that the region experienced appreciable climate change across the K-Pg. Elevated soil temperatures coincide with the maximum values in all soil indices and estimated MAP. Modern soil analogs with similar CIW and Ba/Sr values suggest the landscape of the Songliao Basin was subject to much hotter mean annual air temperatures (MAAT) and high MAP compared to modern conditions, where temperatures currently range from 8 to 24°C (Marbut 1935; Sheldon et al. 2002; Yang 2012; *Qing-Yu et al., 2019)*. Soils with similar CIW values are presently

found on a wide latitudinal gradient, 39°N - 45°S, but are primarily concentrated in warmer lower latitude and equatorial regions, including much of equatorial Africa, Brazil, India (USDA-NCRS, 2022). Over the past century these locations have experienced maximum temperatures averaging 28 to 31 ℃, according to the climate data center (https://climate-adapt.eea.europa.eu/) MAP associated with modern analogs range between 1000 – 1800 mm, with maximum MAP in excess of 3,000 mm/yr (Aparecido et al., 2016; Tadross et al., 2008; Randriamarolaza et al., 2021; Mabrouk et al., 2022). While late Cretaceous MAP does fall within this larger range, it remains near the lower bound of regions that produce soils with similar CIW. Late Cretaceous MAP best agrees with modern soils forming in southeast North America, between 30 – 35°N, and sub-tropical regions of China < 30 °N (Sheldon et al. 2002; Bacon et al., 2012; Bockheim and Hartemink, 2013; Wang et al. 2013) The combination of increased MAAT, MAP, and soil indices suggest the during the LMWE the Songliao Basin resembled a lower latitude subtropical environment.

At the start of early Danian cooling, CIW, Ba/Sr and Al/Si fall near minimum values, expected during a cooler climate. Ba/Sr values fall and remain near 2 which is much closer to commonly observed soil levels of Ba/Sr (Vinogradov, 1959; Retallack, 1990; Terry, 2001). The drop of Al/Si suggests decreased *in situ* clay production that does not rebound. Both indices show abrupt decreases in the lead-up to the Chicxulub impact, while the CIW shows evidence of a more gradual decline that predates the impact. Further support that the soil indices reflect climate-driven soil processes is a brief spike in CIW, Ba/Sr, and Al/Si at 65.88 Mya, during an ephemeral return to pre-impact warming (i.e. covariance between soil proxies and temperature is maintained throughout

the entire dataset). It is notable that Ba/Sr and Al/Si do not covary with shifts in MAP during the Paleogene and raises questions regarding a potential decoupling between the climate signal and CIW (the basis for MAP). This possibility is discussed further below in section 6.5.

Elevated soil indices observed in the late Cretaceous are not in total agreement with spore and pollen data previously interpreted to suggest a more moderate climate (Wang et al. 2013; Gao et al., 1999). The relative percentages of coniferous, deciduous, and herb/shrub plant types present in the Mingshui formation have been used to indicate semi-humid and temperate conditions. This interpretation may agree more closely with trends in this study's kernel smoothed average temperatures and MAP rather than the punctuated periods of discrete temperatures in excess of 27 °C.

Competing interpretations derived from pollen/spore vs. soil/isotopic proxies are not necessarily in conflict. Both signals may represent the integrated history of the basin concatenated within relict and/or polygenic soils. Paleosol and modern soils have been demonstrated to preserve multiple sets of characteristics that are attributable to separate periods of unique climatic or environmental influences that are unrelated to the active influence on a soil for a given time (Fedoroff et al., 2010; Cremaschi et al., 2018). Relict soils, non-buried soils that are still interacting with the atmosphere, are frequently associated with areas that have experienced aridification. Aridification allows for the preservation of soil features previously formed during more humid conditions, without being overprinted or chemically altered as climate changes. The result is that a sequence of paleosols analyzed across an interval may be biased toward wet conditions. Examples include the Atacama Desert where soils have preserved isotopic evidence of steady

aridification in relict Bk horizons; and highly weathered soils found in the Italian Alps that contain spodic horizons, drastically contrasting with the surrounding younger and less pedogenically modified soils formed strictly under the influence of Holocene climate (D'Amico et al., 2016; Ebeling et al., 2016). Given the ~500 mm/yr decline in precipitation over the latest Cretaceous, it is possible that soils within Songliao Basin contain relict features as a function of aridity. Additionally, it is reasonable to suggest a hotter and wetter late Cretaceous increased soil erosion and hindered preservation of pollen and spore assemblages that better reflect the elevated temperatures in this study (Havinga, 1967; Havinga, 1971; Eddudottir et al., 2020; Xue et al., 2023). This period of the latest Cretaceous occurs during a larger occurrence of scant pollen and spore data within the Songliao basin core and has been interpreted to reflect the extinction of key east Asian flora (Li et al., 2011)

6.1.2 Global Correlation

Currently, no compilation of K-Pg terrestrial climate dataset nears the comprehension of Hull et al. (2020), which compiles thousands of marine temperatures from over 20 sites capturing temperature change across low and high latitudes (e.g.- Alegret and Thomas, 2013; Wilf et al., 2003; Li and Keller, 1998; Barnet et al., 2017; Woelder at al., 2018). The result is a largely coherent ~2 ℃ of transient warming and subsequent cooling that precedes the Chicxulub impact. Comparing the Songliao Basin record to both the mean temperature change integrated across latitudes, and to SST records from individual locations nearest to Songliao Basin reveals the need for careful consideration when extrapolating between terrestrial and marine realms. As a whole, the

agreement between the Songliao Basin and marine sites is limited to pre-impact warming, with comparably attenuated temperature change at marine sites. Immediately following the impact marine temperatures fall by 7 ℃, a phenomenon not witnessed in Songliao Basin (Vellekoop et al., 2016). Following the temperature drop early Danian marine temperatures rebound to pre-LMWE temperatures and continue to warm by ca. 1℃ over the next 0.5 Myr (Hull et al. 2020). No period of cooling comparable to what is estimated in Songliao Basin is observed in marine studies. Bulk and planktonic foraminifera temperature records sampled from Pacific Ocean ODP site 1209 are as much as 10℃ cooler than terrestrial temperatures at the K-Pg, and are on average 3 ℃ cooler in the early Danian. The trend is also anticorrelated as site 1209 experienced ~2 ℃ of warming after the Chicxulub impact, during terrestrial cooling. Additionally, ODP 1209 bottom temperatures are more reflective of the average marine trend, including a mild degree of consistent warming throughout the early Danian (Westerhold et al. 2011).

Temperatures reconstructed from Songliao Basin are not terrestrial outliers and point to enhanced continental warming (Byrne and O'Gorman, 2018). Newly published studies sampling from both high and low latitude terrestrial sites substantiate the ample warming and long-term cooling recorded in the Songliao Basin. Regionally, Δ_{47} temperatures reconstructed from paleosol carbonates in the low-latitude Nanxiong Basin suggest the MAAT near the K-Pg averaged 30 ℃ and that summer air temperature was as much as 6 ℃ higher than MAAT (Yin et al., 2023). Additionally, the shift in $\delta^{13}C$ and $\delta^{18}O$ at 66 Ma is observed in both the Songliao and Nanxiong basins with a similar magnitude of change. At higher latitudes (~57°N) in North America, GDGT temperatures derived from peat deposits indicate warming occurred over the last 5 kyr of the

Cretaceous and continued for 10 Kyrs (O'Connor et al., 2023). The change between discrete temperatures exceeds 10 ℃ with a maximum temperature of 29 ℃. Warming is followed by a 5℃ drop in temperature over 20 kyrs, with continued background cooling into the Paleogene. In the North American mid-latitudes (~42° N), Δ_{47} temperatures from bivalves found in the Hell Creek Fm also suggest average temperatures near 30 ℃ during late Cretaceous warming. However, given the different environment it is harder to make a direct comparison between bivalves and landscape-scale records. Additionally, age is poorly constrained across the stratigraphic section which may also explain why dramatic cooling predates the K -Pg at this site.

Overall, terrestrial records across latitudes are remarkably similar. The magnitude and coincidental timing of temperature change across these locations suggest global forcing and the global continuity of the LMWE. The cooling observed in the Danian across all terrestrial sites indicates a significant climate response independent of any teleconnections from the warming marine realm. Additionally, the similarity in the absolute values of temperature across latitudes provides a snapshot view of global atmospheric temperature gradients. Similar temperatures support previously hypothesized weaker latitudinal temperature gradients during the K-Pg (Huber et al., 1995; Huber et al., 2002; O'Connor et al., 2023).

6.2 Drivers of Songliao Climate Change

The increased resolution of temperature change during this period allows for testing two hypotheses: (1) that Deccan Traps volcanism is the primary driver of late Cretaceous warming in the region, and (2) that a high-resolution temperature record will

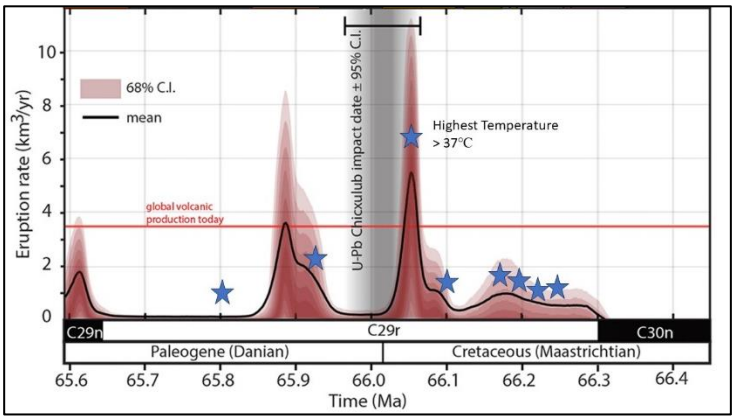

Figure 5. Deccan Traps Chronology with blue stars indicating timing of soil temperatures > 27 ℃ Modified from Schoene et al. (2019)

elucidate current disputes in the timing, rates, and potential episodic nature of eruptivity. There is some difficulty in constraining the impact of the Deccan Traps due to extensive periods of volcanism and prolonged degassing of CO_2 that overall are interpreted to have lasted 700 to 800 kyrs, as well as the inherent error associated with dating methods (e.g., Sprain et al., 2019; Scheone et al., 2019; Nava et al., 2021; Schoene et al, 2021; Baksi, 2022). However, there are currently two dominant chronologies of Deccan Traps eruptions, uniquely identified by their radiometric dating methods. First, the Sprain et al. (2019) Ar/Ar chronology is defined by constant eruptivity averaging nearly 2 km^3/yr. Sprain's eruption rates are consistent and indifferent to the timing of the Chicxulub impact, or the K-Pg more generally. However, the majority of the volume of volcanic material is interpreted to occur post-impact. Alternatively, the chronology by Schoene et al. (2019) based on U-Pb dating produces a much more episodic evolution of Deccan Traps. Superimposed on a based line eruption rate that range from near zero to 0.5 km^3/yr are periods of so-called "main phase" eruptions. The two most vigorous episodes occur almost directly before and after the impact. Prior to the impact, a prolonged low-grade eruption beginning at 66.3 Ma terminates into a short-lived burst potentially 10 km^3/yr

eruption from 66.1 to 66.0 Ma. Following the impact, a potentially milder episode of 3.5 to 8 km^3/yr eruption occurs between 65.9 and 65.8 Ma.

Analogous to the Schoene et al. (2019) interpretation of the eruption timeline, soil temperatures in Songliao Basin illustrate two discrete warming episodes. The highest temperatures occur between 66.23 and 66.1 Mya during the prolonged ramp up period in the first main phase. Soil temperatures drop near mean levels near the time the Chicxulub impact, where Deccan Traps activity is also interpreted to drop to near 0 km^3/yr. Additionally, temperatures rebound between 65.96 and 65.92 Mya, coinciding with the next phase of increased volcanic activity. Across this data set, only one elevated temperature represents an outlier. At 65.80 Mya, a 30 ℃ temperature (interpreted to occur 95 cm in the soil profile) occurs during almost no suspected volcanic activity, and lags the previous main phase eruption by 10kyr's (Fig 5). The timeline of elevated temperatures in this study therefore mostly supports the chronology detailed by Schoene et al. (2019).

Gu et al. (2022) recently published Hg data sampled from the SK-1n borehole at the K-Pg which illustrates further agreement between volcanic forcing and increased temperatures. Hg anomalies are widely used as a proxy for volcanic activity and the global correlation of volcanic events (Thibodeau and Bergquist, 2017; Percival et al., 2018; Grasby et al., 2019; Them II et al., 2019; Shen et al., 2020), In Songliao Basin, background levels of Mercury remain near 6 ppb with the exception of sediments sampled at a core depth between 318 and 326 meters, representing the boundary of the K-Pg. Here, Gu identifies "Spike 1" at 60 ppb (325.8 to 324.0

m), and “Spike 2” at 40 ppb (322.8 m). In this study, the same section of the core contains two temperatures >30 ℃. This section is dated to roughly 66.1 – 66.0 Mya, the same period Schoene et al. (2019) interprets the highest eruption rates.

6.3 Climate, Seasonality, and Possible Artificial Signals in $\delta^{18}O_{pw}$

The Songliao Basin has been a compelling case study for interpreting climate induced changes to regional hydrology, partially due to the basin’s modern latitudinal position at a quasi-convergence zone between westerly, Arctic, and monsoonal derived precipitation (Kong et al., 2016; Chen et al., 2010, Chen et al., 2008; Tian et al., 2001). The basin’s similar paleolatitude in the late Cretaceous, paired with spatially consistent $\delta^{18}O$ records throughout the Cenozoic, has justified an assumption for near modern hydroclimate dynamics, albeit with some important caveats (Caves et al., 2015; Yang et al., 2020). Numerous studies have evoked the modern seasonal change between westerly and monsoonal derived precipitation to explain changes in the $\delta^{18}O_{pw}$ during periods of late Cretaceous climate change (e.g. – Gao et al. 2015a; 2021; Zhang et al., 2018; Chen et al., 2022). The change in precipitation source is based on observed ~3‰ shifts in $\delta^{18}O_{pw}$ that mirror the magnitude of modern interannual variation in $\delta^{18}O$ of precipitation ($\delta^{18}O_{precip}$; Araguás-Araguás et al., 1998). During colder months when westerly precipitation dominants, precipitant is derived from artic source waters producing a $\delta^{18}O_{precip}$ ~3‰ lower relative to monsoonal derived precipitation (Araguás-Araguás et al., 1998; Li et al., 2012). Zhang et al. (2018) has also posited that the presence of pedogenic carbonate is itself evidence of an established monsoonal climate that was seasonally dry (Khormali et al., 2020). The dominant smectite clay mineralogy may also suggest some

degree of seasonality (Gao et al., 2015b; Meyers and Tabor, 2015). However, combining data in our study with previous records highlights the need to interrogate the robustness of relying on modern precipitation analogs to explain the late Cretaceous $\delta^{18}O_{pw}$ record (following up on interrogation of this issue by Gao et al. (2021)).

In the lead up to the K-Pg. Zhang (2018) reconstructed nearly 4‰ enrichment in $\delta^{18}O_{pw}$, estimating a shift from approximately -10‰ (~67 Ma) to -6‰ (~66 Ma). As in previous studies, Zhang interprets the change as a shift from westerly to monsoon-derived precipitation. However, our study shows the same degree of enrichment continuing after the K-Pg, approximately -8‰ to -4‰. Combining this study with Zhang et al. (2018) results in ~6‰ of sustained enrichment from 67 to 65 Ma, essentially double the enrichment attributed to modern seasonal source water variation. We first look for alternative explanations to explain trends in $\delta^{18}O_{pw}$ and then further discuss issues with the modern-paleo comparison.

Plotting $\delta^{18}O_{pw}$ against the decompacted soil profile depth of each sample, Gao et al. (2021) demonstrates consistent enrichment of in $\delta^{18}O_{carb}$ and $\delta^{13}C_{carb}$ in shallow formed carbonates, highlighted the potential for evaporative induced enrichment of soil porewater prior to carbonate formation. We build on this previous analysis by combing the results of our study with $\delta^{18}O_{pw}$ values calculated using our new soil temperature record (e.g. - Huang et al., 2013; Gao et al., 2015a) and bin the total data set by 10 cm intervals (Fig 6L). We then identify where shallow-formed samples occur on our time series and access the impact evaporative enrichment may have on the $\delta^{18}O_{pw}$ record (Fig 6R). Binning $\delta^{18}O_{pw}$ by depth results in statically significant enrichment in samples formed above 60 cm (*t = -3.5473, p-value = 0.0001*). Samples below 60 cm converge on

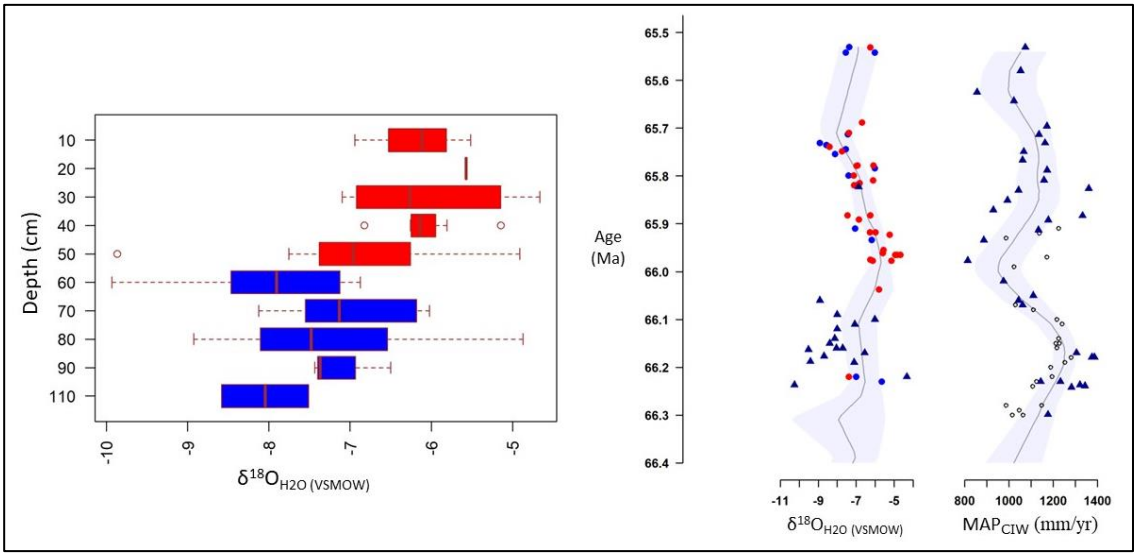

Figure 6. Left: Compilation of new and previously reconstructed δ^{18}Opw illustrating statistically significant enrichment in carbonates formed above 60 cm depth, Right: Red dots represent data from shallow formed carbonates, highlighting that the apparent ~3‰ shift may be an artifact of evaporative enrichment where triangles = matrix and dots = nodules

a mean of -7.34‰ mean with nearly 3‰ enrichment found in samples formed at a depths < 30 cm. We interpret enrichment above 60 cm as potentially resulting from evaporative enrichment. Shallow carbonates occur between 66.0 and 65.7 Ma and present as a gradual ~ 3‰ excursion that return to pre-excursion values at 65.73 Ma. The initial enrichment occurs contemporaneously with decreasing MAP. Importantly, depth-to-carbonate is itself a proxy for MAP independent of the CIW method utilized in this study (Retallack, 2005). Thus, decreasing MAP_{CIW} during a decreased depth-to-carbonate and $\delta^{18}O_{pw}$ enrichment strengthens an interpretation for aridity induced evaporative enrichment

Without the context of sample depth and the potential for evaporative enrichment, the overall $\delta^{18}O_{pw}$ trend is similar to trends previously interpreted as indicating changes in precipitation source. After removing these samples from consideration, the remaining

data remains near the -7.34‰ mean, albeit with some spread in the data, and lacks any apparent trends or sustained shifts in $\delta^{18}O_{pw}$. Our study demonstrates the possibility for evaporative enrichment to obscure the $\delta^{18}O_{pw}$ signal and mimic changes in source water. Given the potential impact this has on our study's $\delta^{18}O_{pw}$ record, we deem it is necessary to reevaluate the regional $\delta^{18}O_{precip}$ more generally and interrogate if modern $\delta^{18}O_{precip}$ is substantially unique to source water.

The late Cretaceous was a pre-Himalayan world and the elevation of the Tibetan Plateau remained under 1,000 m (An et al., 1999; Li, 1999; Ibarra et al., 2023). As a result, eastern Asia did not have a topographic barrier attenuating the westerly jet stream and was therefore primarily under the influence of westerly-sourced precipitation (Zhang, 1995; Liu et al., 1998). Some arguments suggest that coastal regions also experienced a paleo-monsoon (Jiang and Li, 1996; Ohba and Ueda, 2010; Yang et al. 2020). However, it is important to highlight the that Songliao Basin represents the furthest continental (and northward) extent of monsoonal moisture (Gao et al., 1962; Tian et al., 2001 Tang et al. 2006; Hu and Qian, 2007; Chen et al., 2008; Chen et al., 2010;). Therefore, in the absence of a modern Tibetan plateau it may be possible the continental extent of the monsoon was forced coastward under the influence of a stronger westerly current. Kong et al.'s (2019) updated classification scheme for precipitation zones across China, which builds on the work of Araguás-Araguás (1998), Huang (1959), and Luo (1954) offers spatial context for $\delta^{18}O_{precip}$ and enables an updated comparison of regional precipitation signals. We compare $\delta^{18}O_{precip}$ along a west-east transect at ~40°N where elevation is largely stable between 1500 and 2000m (Caves et al., 2015). The boundary delineating westerly and artic precipitation regions is found near 90 – 100°E, and the boundary

separating Arctic and Pacific precipitation zones is between 110 – 120 °E. At this latitude, the annual average of $\delta 18O_{precip}$ between westerly and Arctic ranges from -11 to -6‰. In both regions, the late summer $\delta 18O_{precip}$ ranges between -10‰ and -5‰, during the annual period of carbonate formation (Breeker et al., 2009). The range in both data sets overlap with the ranges found in Zhang et al (2018) during the K-Pg and in our study. Additionally, Yang et al. (2017) compiled monthly records of $\delta^{18}O_{pw}$ from 1979 to 2007 using six simulations of isotope enabled general circulation models. The precipitation zones differ from Kong et al. (2019), however, the results confirm late summer overlap in $\delta^{18}O_{precpip}$ between westerly, artic, and monsoonal moisture in all models. Source water has been designated the most important factor in determining $\delta^{18}O_{precip}$ (Liu et al., 2014; Li et al., 2014; Kong et al., 2019), and given similar elevations across this transect, we determine seasonality in westerly and Arctic source waters is a potential alternative explanation for observed shifts in late Cretaceous $\delta^{18}O_{pw}$, especially when considering a stunted Tibetan plateau and a stronger westerly flow across Eurasia. As such, we suggest further study of a potential late Cretaceous paleo-monsoon (e.g., Yang et al., 2020; Ma et al., 2021 Li et al., 2022) is warranted.

While the presence of carbonate and smectite do support some degree of seasonality in Songliao Basin, the complexities of linking $\delta^{18}O$ values to precipitation source, and the potential for evaporative enrichment obscuring an accurate signal, indicate that shifts in $\delta^{18}O_{pw}$ between should be cautiously interpreted. However, more substantial changes in $\delta^{18}O_{pw}$ are a potentially robust indicator of global processes unbiased by seasonality. The longer $\delta^{18}O_{pw}$ record (76 to 66 Ma) most recently compiled by Gao et al. (2021) illustrates changes on the order of -14‰ to -6‰ during a transitions

between cold and warm periods, and interprets the excursion as the poleward movement of atmospheric cells and a global change in the hydrologic cycle. In these scenarios, the degree of change is not only more substantial, but the depleted values are stable throughout the cold period and enriched values are sustained during warm periods. Regardless, in all scenarios, the depth of carbonate nodules should be considered when interpreting $\delta^{18}O_{pw}$.

6.4 Soil Respiration and Ecosystem Productivity

6.4.1 Soil Respiration and Climate

In this section we limit discussion to the novel SR estimates produced only in this study due to significant variation from previous studies, which we discuss below. SR is interpreted in the context of modern biomes based on (1) soil classification and pollen proxies that suggest a temperate forest analog, and (2) climate and weathering proxies which reflect a lower latitude subtropical biome. Comparing the Songliao Basin to a comprehensive compilation of SR rates between 1971 and 2000 reveals tropical and temperate biomes as the two best fit modern analogs (Bond-Lamberty and Thompson, 2010). Tropical and temperate biomes share a similar spread in SR rates (500 to 3000 gC $m^{-2}yr^{-1}$) with the highest frequency SR occurring near ~1000 gC $m^{-2}yr^{-1}$. SR in both biomes contain a right skew and with very low frequency data near the maximum values (>2500 gC $m^{-2}yr^{-1}$). All of these characteristics are observed in the Songliao Basin dataset. SR respiration rates for modern subtropical biomes are skewed lower and do not suggest similar productivity levels to the Songliao Basin.

With these modern analogs determined, we consider the influence of elevated pCO_{2atm} during the K-Pg on productivity. Based on the paleCO2 database, the latest Cretaceous pCO_{2atm} ranges from 1090 to 950 ppm, more than double modern conditions (Hönisch, 2023; Tans and Keeling, 2023). During this period mean SR is 1350 ±579 gC $m^{-2}yr^{-1}$. The mean annual SR for modern temperate, subtropical, and tropical biomes are approximately 745 ± 421 , 776 ± 380, and 1286 ± 633 g C m^{-2}, respectively (Hudgens and Yavitt, 1997; Billes et al. 1971; Bond-Lamberty and Thompson, 2010). At this time, SR is most reflective of modern tropical conditions despite the latitudinal difference and a lack of pedological and vegetative evidence for tropical conditions. However, numerous field and laboratory studies have demonstrated the potential for increased SR under elevated CO2 (Johnson et al., 1994; Saxe et al., 1998; Norby et al., 1999; Motha and Bier 2005). Forest ecosystems show the greatest potential for increased productivity due to CO_2 effects. Upwards of 60% stimulation in photosynthesis has been observed when CO_2 is increased twofold (REFS) and supports the idea that the Songliao Basin was likely a highly productively temperature forest ecosystem with relatively high SR driven by increased pCO_{2atm}. Notably, studies have determined the potential for plant acclimation and diminished productivity in the years following increased CO_2 conditions, thus leaving open the possibility that both past and modern SR fall somewhere within margin of error and that actual increases in SR are milder (Luo et al., 2001; Rustad et al., 2001; Melillo et al., 2002; Strömgren, 2001).

The most striking characteristic in the late Cretaceous is continual SR decline between 66.22 and 66.09 Ma. SR decreases 1,471gC $m^{-2}yr^{-1}$, from 2,236 to 764 gC $m^{-2}yr^{-1}$. There are several compounding factors that may lead to SR decline. Temperature and

soil moisture are considered the most significant factors in SR (Lloyd and Taylor, 1994; Bowden et al., 1998; Davidson et al., 2006; Gaumont-Guay et al., 2006b; Curiel-Yuste et al., 2007; Yan et al., 2019) MAP declines by 686 mm/yr, indicating that water stress may be a significant contributing factor to SR declines. The elevated temperatures coinciding with increased aridity may compound stress on productivity. While modern observations indicate a global increase in SR potentially linked to rising temperatures, highly elevated temperatures may cause plants to underutilize CO2 a lead to a decrease in net growth (Rosenzweig and Hillel, 1995; Motha and Bier 2005; Bronson et al., 2008;). Since soil temperatures during this period are likely an underestimate, MAAT may be near or at 40°C and the resulting combination of high temperatures and water stress may have been extreme enough to force the late Cretaceous ecosystem outside of optimal conditions. Additional support for aridity-forced declines in SR are late Cretaceous enriched $\delta^{13}C_{org}$ (-24 to -22‰). These are notably enriched values for the C3 interpreted to be the dominant plant type at this period. However, they near the 25‰ measured in the lower Nenjiang Formation and can be explained by water stress (Tipple and Pagani, 2007; Kohn 2010; Song et al., 2013; Montañez, 2013; Caves et al., 2016). During periods of water stress plants will close their stomatal openings and consequently have lower internal CO_2 concentrations. This action reduces the discrimination between carbon isotopes and results in a more positive $\delta^{13}C_{org}$. Additionally, $pCO2_{atm}$ declines by 142 ppm during this period. Field and laboratory studies have shown SR is affected by changes in CO2 on a similar order (175 - 300 ppm) supporting evidence of $pCO2_{atm}$-driven decline in SR (Vose et al., 1995; Bernhart et al., 2006). The late Cretaceous decline in SR predates the timing of the Chicxulub impact. Near the boundary there are

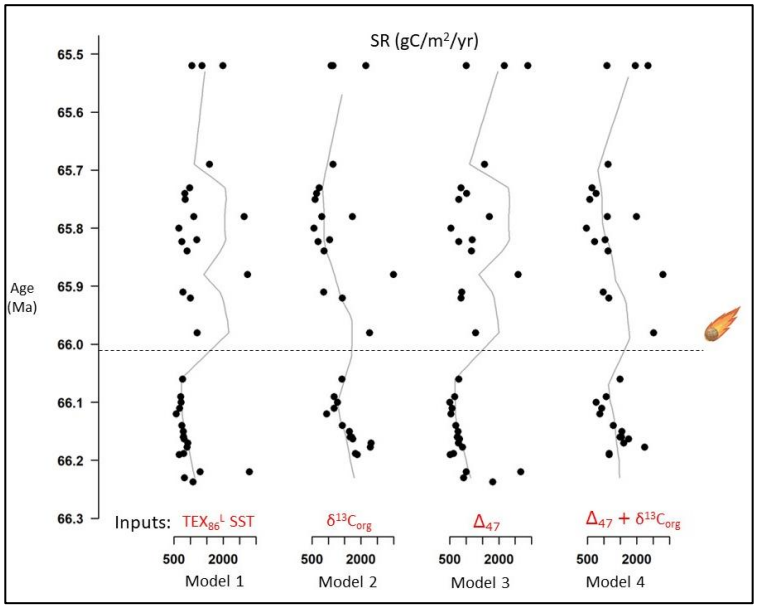

Figure 7. Time series data for each SR model with inputs in red. $\delta^{13}C_{org}$ used to estimate $\delta^{13}C_{\theta}$; temperature used to calculate fractionation factor between $\delta^{13}C_{carb}$ and soil CO2 (as explained in section 3); Chicxulub impact 66.05 ± 0.031 Ma

no additional or abrupt decreased in SR and no evidence for impact induced decline in productivity. Instead, early Danian SR continues to decrease and overall ranges between 500 and 1000, closer to modern temperate and subtropical environments (Billes et al. 1971; Bond-Lamberty and Thompson, 2010). This occurs while pCO_{2atm} continues to decline supporting the hypothesis of CO_2 forcing on either of these biomes.

6.4.2 Soil Respiration Model Comparisons

Our study builds on previous attempts to model SR in Songliao Basin by decreasing the number of assumed variables with an increased the number of in-situ coeval measurements (Δ_{47} temperature and $\delta^{13}C_{org}$). To evaluate the impact on these updated variables we run four simulations (Fig 7) on our dataset. Model 1 follows the same parameters as Gao et al. (2015a), who used to estimate SR in Songliao Basin i.e., temperature is based on the SST record of Linnert et al. (2014), and δ_{θ} is estimated using

a fixed $\delta^{13}C_{org}$ of -25‰ based on the underlying Nenjiang Formation (Song et al., 2013); model 2 replaces only the fixed δ_θ with our $\delta^{13}C_{org}$ record; model 3 replaces only the SST with our soil temperature record; and model 4 contains both the measured $\delta^{13}C_{org}$ and soil temperatures. $pCO2_{atm}$ values are derived from the paleoproxy CO2 database and remain constant across all models.

The mean values for models 1-4 are: 735, 1605, 679, and 1349 gC $m^{-2}yr^{-1}$, respectively. All four models produce SR estimates higher than Gao et al.'s (2015a) estimated mean for the same time period, ca. 500 gC $m^{-2}yr^{-1}$. SR rates in Gao et al. (2015a) are well below most reasonable modern analogs with the majority of SR rates < 500 gC $m^{-2}yr^{-1}$. Based on the Gao et al. (2015a) dataset, the best fit modern analog is either an Arctic or boreal biome. No data in previous Songliao Basin studies resemble these environments. We consider (Gao et al., 2015a) to represent a systematic underestimate in SR and stress the importance of maximizing *in situ* measurements when possible. Given that Model 1 also estimates slightly higher SR relative to Gao et al. (2015a), the paleoCO_2 dataset must also drive some of the increased SR rates. Overall, the increased SR values derived from models 2 and 4 suggest the potential for high sensitivity to δ_θ (Fig. 8).

Table 1. Inputs and Mean SR values from 4 modeling scenarios. All Models include the same pCO_{2atm} values selected from the paleoCO2 database (Honisch, 2023)

Model	**1**	**2**	**3**	**4**
Variables (Estimated)	SST, $\delta^{13}C_{org}$	SST	$\delta^{13}C_{org}$	/
Variables (In-situ)	/	$\delta^{13}C_{org}$	Δ_{47}	$\delta^{13}C_{org}$, Δ_{47}
Mean (gC m-2yr-1)	735	1605	679	1349

The largest discrepancy between the four simulations in the study is amount of decline in the in the late Cretaceous (Fig 7). Models 1 and 3 show a lesser degree of

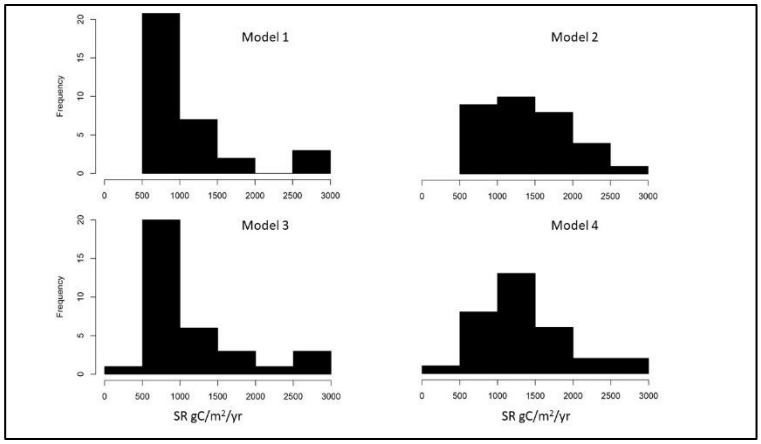

Figure 8. Distribution of total SR rates for the entire K-PG time period in each model. Model 1 = TEX_{86}^{L} SST and no in situ data, Model 2= TEX86L SST and in situ $\delta^{13}C_{org}$, Model 3= Δ_{47} soil temperature , Model 4= $\delta^{13}C_{org}$ Δ_{47} soil temperature

decline between 66.22 and 66.09 Ma., -349 and -394 $gCm^{-2}yr^{-1}$, respectively. The overall similarity between Model 1 (SST) and Model 3 (Δ_{47}) highlights that the temperature used to calculate the fractionation factor between $\delta^{13}C_{carb}$ and $\delta^{13}C_s$ has a relatively smaller impact on SR. Additionally, samples that have elevated soil temperatures (>27°C) do not result in outlier SR estimates. Models 2 and 4 both include an exaggerated change in SR late Cretaceous decline SR, declining by 1,329 and 1,471 gC $m^{-2}yr^{-1}$, respectively. An exaggerated decline seems to represent the greatest agreement with climate proxies, given continually increasing aridity and high temperatures over the decline. However, model 2 far exceeds the mean SR for all modern biomes indicating in-situ soil temperatures exert an important attenuating influence on SR.

6.5 Considerations and Problems with Soil-Type Interpretation

The average CIW associated with modern Alfisols falls within 69.1 ± 8 while the majority of Songliao Basin samples fall above 80 (Sheldon et al., 2002; Sheldon et al., 2009). This discrepancy calls for interrogating the current Alfisol classification. Importantly, Gallagher and Sheldon (2016) have demonstrated that soil taxonomy has no impact on the Δ_{47} temperatures derived from soil carbonates. As such, any updated

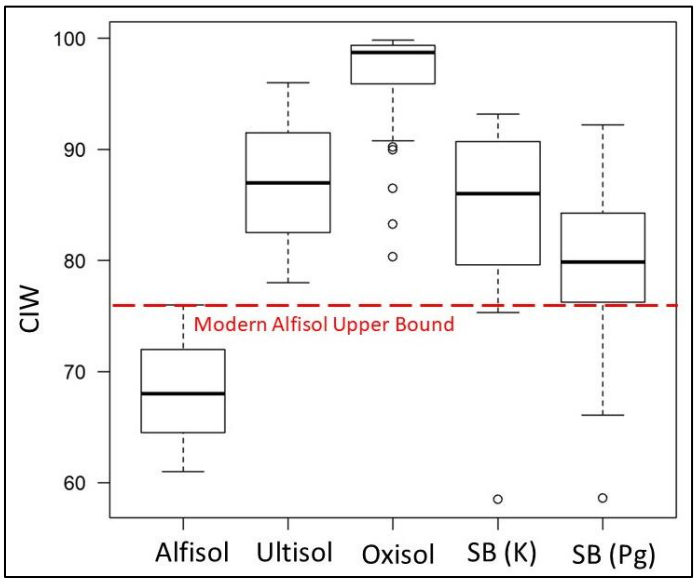

Figure 9. CIW values for modern soils compare to Late K and early Pg paleosols in the Songliao Basin (SB)

interpretation of the pedological and sedimentological composition on the basin do not necessitate a reinterpretation or reexamination of temperature change, nor does it necessitate recalculation of $\delta^{18}O$ porewater or SR estimates. We acknowledge that Kelson et al. has demonstrate the impact of coarse grained soils on Δ_{47}, however coarse grained is defined in their study as majority gravel (> 50%). Sediments in our study are siltstone or finer. With these caveats in mind, it is important to explore potential problems with the current Alfisol classification and larger repercussions of that previous classification.

Two possible hypotheses may explain the elevated CIW values in Songliao Paleosols: (1) Alfisol is the incorrect modern analog to associate with Songliao paleosols, or (2) geochemical proxies does not represent a climatically forced pedogenic signal, and thus reflects a depositional/provenance signal but the soil type designation remains correct. Modern analogs with CIW values in the range of Songliao Basin are designated as Ultisols and Oxisols. As discussed above, Ultisols have a larger latitudinal spread, both are largely concentrated in tropical and low latitude environments and experience average annual and summer temperatures of these locals are more reflective of the soil temperatures in this study (Aparecido et al., 2016; Tadross et al., 2008; Bockheim and

Hartemink, 2013; Randriamarolaza et al., 2021; Mabrouk et al., 2022). Additionally, Ba/Sr in the late Cretaceous is reflective of Oxisolic conditions and extremely elevated compared to both modern Alfisols (Ba/Sr > >10) and Ultisols (Ba/Sr ~ 10) (Terry, 2001).

The argument for the CIW signal as being influenced by provenance is supported by both disagreement between various geochemical and mineralogical proxies, and the confounding factor of *time of soil formation.* First, the majority of CIW values from these paleosol fall into the bin of Ultisol. In terms of clay mineralogy, Ultisols are defined by the presence of kandic horizons that are associated with high amounts kaolinite and other high weathering product minerals (Eswaran and Sys, 1979, Okusami et al., 1997, Shaw et al., 2004; Bockheim and Hartemink, 2013:) Alfisols however, are found with high amounts of smectite, often reflecting more seasonal and moderate climatic conditions. (Trakoonyingcharoen et al., 2006; Tabor and Myers, 2015). A review of XRD analysis of Ultisols and Oxisols across a wide latitudinal transect illustrates consistently dominant peaks in the 3, 7, and 12 2θ regions for both soil orders, and demonstrates that kaolin minerals are a strong marker for the presence of Ultisols and Oxisols. Previous analysis of Songliao Basin paleosols show only trace amounts of kaolinite, which have been attributed to diagenesis (Gao et al., 2015b). Additionally, there is an issue regarding relative amounts of clay. The agreement between CIW and Al/Si seen in this study is expected as secondary clay minerals form from increased weathering. As such, soil indices indicate the late Cretaceous should be period of relatively high amounts of clay. Gao et al. (2015b; 2021b) XRD analysis quantifying the ratio between total clay and quartz does not produces such results. Between 66.2 and 65.5 Ma the index ranges between 20 to 100, with no trend or covariance with geochemical proxies. Additionally,

the spread within the data is persistent across the time entire interval. The highest Al/Si values in the late Cretaceous occur with some of the lowest clay:quartz values. Although Ultisols and Oxisols have a larger component of siliceous minerals, both still contain appreciable amounts of clay. Climate, mineralogy, and geochemistry do not converge a clear soil order.

Time of soil formation suggests a larger problem with the application of any of these three soil orders furthering support for interpreting CIW as a provenance signal. Alfisols, the least pedogenically modified of the three soil orders, are associated with a minimum formation time of 10 kyr, and are frequently interpreted to require 100+ kyr. Clay rich argillic horizons are posited to require up to 300 kyr of soil development (Birkeland, 1984). Gao (2015b) interprets both smectic and illite in this section of the Songliao Basin core to represent authigenic climate-driven clay production, indicating the presence of an argillic horizon. An argillic horizon would suggest formation time closer to the upper bound of the 10 – 300 kyr range. The lack of any K horizons (fully indurated carbonate horizons) constrain formation time to < 400 kyr. To consider how relates to current age model for the Songliao Bain, we can remove moving matrix samples from consideration and base the chronology of soil formation on the age and stratigraphic placement of soils from previous studies (e.g. - Gao et al., 2021) that only consider soils bearing carbonate nodules. The frequency of Alfisols therefore occur at 1 -2 kyr intervals across the K-Pg. If even possible, the conditions needed for such intense pedogenesis should result in high amounts of iron oxides and kaolin group minerals that are not present in any soils. Furthermore, soils formed under these conditions are not reflective of seasonality and lack conditions suitable for carbonate nodule formation.

Provenance presents as a reasonable explanation for these confounding factors when the tectonic and sedimentological history is considered. The long-lived lake basin at Songliao accumulated high yields of sediment prior to tectonic uplift in the Cretaceous, including abundant volcaniclastic material (Gao et al. 2013; Wang et al. 2013; Gao et al 2015a). These sediments easily weather to clay and would subsequently continue to weather while reworked and redeposited as uplift altered the focus of deposition within the Basin (Wilson and Pittman, 1977; Cuadros et al., 1999; Fesharaki et al., 2007; Feng et al., 2010; Franke and Ehrmann, 2010; Li et al., 2010; Wang 2013). The surrounding Lesser Xing'an-Zhangguangcai range, a source a sediment during the deposition of the Mingshui formation, are interpreted to be tectonic stability during deposition (Feng et al., 2010; Li et al., 2010). Stability suggests three is no large in-flux of physically weathered sediment and supports a hypothesis that the majority of sediment is reworked from within the basin. Continued weathering and reworking of easily weathered volcaniclastic minerals and secondary clays offer a reasonable mechanism for increasing CIW by means other than pedogenesis.

7. Conclusion

The Songliao Basin is an important archive of the Cretaceous world that has provided deep insight to many climatic periods. Our study has demonstrated the ability to analyze the basin's history at an even finer resolution and with these insights we have brought new global context to mid-latitude terrestrial climate change during the K-Pg. Our updated temperature record clearly illustrates a direct response to changing eruption rates from the Deccan Traps. The timing between our record and Deccan Traps, in

combination with the coherency between the Songliao Basin and other global terrestrial sections, indicates a strong likelihood that the Late Maastrichtian Warming Event was directly forced by variable volcanic pulses. During this period, soil and isotopic proxies both indicate that the Songliao Basin resembled a warmer lower latitude environment that fostered a highly productive ecosystem. Soil respiration rates were much greater than similar modern environments which we attribute to elevated $pCO2_{atm}$. We have updated the SR record with a greater number of in situ measurements which resulted in a significant overall increase in SR and demonstrated improved agreement with climate proxies. Our study considers potential obscuring factors by pointing out the persistent problem of evaporative enrichment on the $\delta^{18}O_{pw}$ record and the ambiguity in correlating calculated $\delta^{18}O_{pw}$ to modern precipitation sources (and seasonality). Based on this work, future studies should consider the impact of sediment reworking on soil proxies and paleosol classification and the impact on paleoclimate interpretation. Lastly, future studies will continue to test the potential and efficacy of analyzing soil matrix carbonates in comparison to carbonate nodules to increase the temporal resolution and spatial coverage of terrestrial isotopic records derived from paleosols.

References

Abell, J.T., Winckler, G., Anderson, R.F. and Herbert, T.D., 2021. Poleward and weakened westerlies during Pliocene warmth. Nature. 589, 70-75.

Adlan, Q., Davies, A.J. and John, C.M., 2020. Effects of oxygen plasma ashing treatment on carbonate clumped isotopes. Rapid Communications in Mass Spectrometry. 34.

An, Z. and John, E., K., Warren L, P., & Stephen C, P.(2001). Evolution of Asian monsoons and phased uplift of the Himalaya–Tibetan plateau since Late Miocene times. Nature. 411, 62.

Anderson, N.T., Kelson, J.R., Kele, S., Daëron, M., Bonifacie, M., Horita, J., Mackey, T.J., John, C.M., Kluge, T., Petschnig, P. and Jost, A.B., 2021. A unified clumped isotope thermometer calibration (0.5–1,100 C) using carbonate-based standardization. Geophysical Research Letters. 48

Alegret, L., Thomas, E., 2013. Benthic foraminifera across the Cretaceous/Paleogene boundary in the Southern Ocean (ODP Site 690): Diversity, food and carbonate saturation. Marine Micropaleontology. 105, 40-51.

Amiot, R., L´ecuyer, C., Buffetaut, E., Fluteau, F., Legendre, S., Martineau, F., 2004. Latitudinal temperature gradient during the Cretaceous Uer Campanian–Middle Maastrichtian: δ18O record of continental vertebrates. Earth Planet. Sci. Lett. 226, 255–272.

Aparecido, L.E.D.O., Rolim, G.D.S., Richetti, J., Souza, P.S.D. and Johann, J.A., 2016. Köen, Thornthwaite and Camargo climate classifications for climatic zoning in the State of Paraná, Brazil. Ciência e Agrotecnologia. 40, 405-417.

Araguás-Araguás, L., Froehlich, K., and Rozanski, K., 1998, Stable isotope composition of precipitation over southeast Asia: Journal of Geophysical Research. 103, 28721–28742.

Barnet, J.S.K., 2019. A high-fidelity benthic stable isotope record of Late Cretaceous Early Eocene climate change and carbon-cycling. Paleoceanography and Paleoclimatology 34, 672-691.

Baksi, A.K., 2022. Critical assessment of the geochronological data on the Deccan traps, India: Emphasis on the timing and duration of volcanism in sections of tholeiitic basalts. Journal of Earth System Science. 131, 135.

Bernasconi, S.M., Müller, I.A., Bergmann, K.D., Breitenbach, S.F., Fernandez, A., Hodell, D.A., Jaggi, M., Meckler, A.N., Millan, I. and Ziegler, M., 2018. Reducing uncertainties in carbonate clumped isotope analysis through consistent carbonate-based standardization. Geochemistry, Geophysics, Geosystems. 19, 2895-2914.

Bernasconi, S.M., Daëron, M., Bergmann, K.D., Bonifacie, M., Meckler, A.N., Affek, H.P., Anderson, N., Bajnai, D., Barkan, E., Beverly, E. and Blamart, D., 2021. InterCarb: A community effort to improve interlaboratory standardization of the carbonate clumped isotope thermometer using carbonate standards. Geochemistry, Geophysics, Geosystems. 22.

Bernhardt, E.S., Barber, J.J., Pippen, J.S., Taneva, L., Andrews, J.A. and Schlesinger, W.H., 2006. Long-term effects of free air CO 2 enrichment (FACE) on soil respiration. *Biogeochemistry*, *77*, pp.91-116.

Bestland, E.A., 2000. Weathering flux and CO2 consumption determined from palaeosol sequences across the Eocene–Oligocene transition. Palaeogeography, Palaeoclimatology, Palaeoecology. 156, 301-326.

Bigeleisen, J. and Mayer, M.G., 1947. Calculation of equilibrium constants for isotopic exchange reactions. The Journal of Chemical Physics. 15, 261-267.

Billes, G., Cortez, J. and Lossaint, P., 1971. Activite biologique des sols dans les ecosystemes mediterraneens. I. Mineralisation du carbone. Rev Ecol Biol Sol.

Birkeland, P.W., 1984. Soils and geomorphology. Oxford university press.

Bond-Lamberty, B. and Thomson, A., 2010. A global database of soil respiration data. Biogeosciences. 7, 1915-1926.

Bowden, R.D., Newkirk, K.M. and Rullo, G.M., 1998. Carbon dioxide and methane fluxes by a forest soil under laboratory-controlled moisture and temperature conditions. Soil Biology and Biochemistry. 30, 1591-1597.

Brand, W.A., Assonov, S.S. and Coplen, T.B., 2010. Correction for the 17O interference in δ (13C) measurements when analyzing CO2 with stable isotope mass spectrometry (IUPAC Technical Report). Pure and Alied Chemistry. 82, 1719-1733.

Breecker, D.O., Sharp, Z.D. and McFadden, L.D., 2009. Seasonal bias in the formation and stable isotopic composition of pedogenic carbonate in modern soils from central New Mexico, USA. Geological Society of America Bulletin. 121, 630-640.

Breitenbach, S.F., Mleneck-Vautravers, M.J., Grauel, A.L., Lo, L., Bernasconi, S.M., Müller, I.A., Rolfe, J., Gázquez, F., Greaves, M. and Hodell, D.A., 2018. Coupled Mg/Ca and clumped isotope analyses of foraminifera provide consistent water temperatures. Geochimica et Cosmochimica Acta. 236, 283-296.

Bockheim, J.G. and Hartemink, A.E., 2013. Distribution and classification of soils with clay-enriched horizons in the USA. Geoderma. 209, 153-160.

Bronson, D.R., Gower, S.T., Tanner, M., Linder, S. and Van Herk, I., 2008. Response of soil surface CO2 flux in a boreal forest to ecosystem warming. Global Change Biology. 14, 856-867.

Byrne, M.P. and O'Gorman, P.A., 2018. Trends in continental temperature and humidity directly linked to ocean warming. Proceedings of the National Academy of Sciences, 115, 4863-4868.

Caves, J.K., Winnick, M.J., Graham, S.A., Sjostrom, D.J., Mulch, A. and Chamberlain, C.P., 2015. Role of the westerlies in Central Asia climate over the Cenozoic. Earth and Planetary Science Letters. 428, 33-43.

Caves, J.K., Moragne, D.Y., Ibarra, D.E., Bayshashov, B.U., Gao, Y., Jones, M.M., Zhamangara, A., Arzhannikova, A.V., Arzhannikov, S.G. and Chamberlain, C.P., 2016. The neogene de-greening of central Asia. Geology. 44, 887-890.

Cerling, T.E., 1984. The stable isotopic composition of modern soil carbonate and its relationship to climate. Earth and Planetary science letters. 71, 229-240.

Cerling, T.E. and Quade, J., 1993. Stable carbon and oxygen isotopes in soil carbonates. Geophysical Monograph Series. 78, 217-231.

Chamberlain, C.P., Mix, H.T., Mulch, A., Hren, M.T., Kent-Corson, M.L., Davis, S.J., Horton, T.W., and Graham, S.A., 2012, The Cenozoic climatic and topographic evolution of the western North American Cordillera: American Journal of Science. 312, 213–262

Chen, F., Yu, Z., Yang, M., Ito, E., Wang, S., Madsen, D.B., Huang, X., Zhao, Y., Sato, T., Birks, H.J.B. and Boomer, I., 2008. Holocene moisture evolution in arid central Asia and its out-of-phase relationship with Asian monsoon history. Quaternary Science Reviews. 27, 351-364.

Chen, F.H., Chen, J.H., Holmes, J., Boomer, I., Austin, P., Gates, J.B., Wang, N.L., Brooks, S.J. and Zhang, J.W., 2010. Moisture changes over the last millennium in arid central Asia: a review, synthesis and comparison with monsoon region. Quaternary Science Reviews. 29, 1055-1068.

Chen, H.F., Liu, Y.C., Chiang, C.W., Liu, X., Chou, Y.M. and Pan, H.J., 2019. China's historical record when searching for tropical cyclones corresponding to Intertropical Convergence Zone (ITCZ) shifts over the past 2 kyr. Climate of the Past. 15, 279-289.

Chen, J., Gao, Y., Ibarra, D.E., Qin, J. and Wang, C., 2022. Mid-latitude precipitation in East Asia influenced by a fluctuating greenhouse climate during the latest Cretaceous through the earliest Paleogene. Global and Planetary Change. 216, 103900.

Cox, A.A. and Keller, C.B., 2023. A Bayesian inversion for emissions and export productivity across the end-Cretaceous boundary. Science. 381, 1446-1451.

Cremaschi, M., Trombino, L. and Zerboni, A., 2018. Palaeosoils and relict soils: A systematic review. Interpretation of micromorphological features of soils and regoliths. 863-894.

Cuadros, J., Caballero, E., Huertas, F.J., Cisneros, C.J.d., Huertas, F., and Linares, J., 1999. Experimental alteration of volcanic tuff: Smectite formation and effect on 18O isotope composition. Clays and Clay Minerals. 47, 769-776.

Curiel Yuste, J., Ma, S. and Baldocchi, D.D., 2010. Plant-soil interactions and acclimation to temperature of microbial-mediated soil respiration may affect predictions of soil CO 2 efflux. Biogeochemistry. 98, 127-138.

D'Amico, M.E., Catoni, M., Terribile, F., Zanini, E. and Bonifacio, E., 2016. Contrasting environmental memories in relict soils on different parent rocks in the south-western Italian Alps. Quaternary International. 418, 61-74.

Davidson, E.A., Janssens, I.A. and Luo, Y., 2006. On the variability of respiration in terrestrial ecosystems: moving beyond Q10. Global change biology. 12, 154-164.

Davies, A.J., Davis, S. and John, C.M., 2021. Evidence of taxonomic non-equilibrium effects in the clumped isotope composition of modern cephalopod carbonate. Chemical Geology. 578, 120317.

Deng, C.L., He, H.Y., Pan, Y.X., Zhu, R.X., 2013. Chronology of the terrestrial Uer Cretaceous in the Songliao Basin, Northeast Asia. Paleogeogr. Paleoclimatol. Paleoecol. 385, 44–54.

Dennis, K.J., Affek, H.P., Passey, B.H., Schrag, D.P. and Eiler, J.M., 2011. Defining an absolute reference frame for 'clumped'isotope studies of CO2. Geochimica et Cosmochimica Acta. 75, 7117-7131.

Du, X., Xie, X., Lu, Y., Ren, J., Zhang, S., Lang, P., Cheng, T., Su, M. and Zhang, C., 2011. Distribution of continental red paleosols and their forming mechanisms in the Late Cretaceous Yaojia Formation of the Songliao Basin, NE China. Cretaceous Research. 32, 244-257.

Du, K., Li, F., Qiao, Y., Leng, P., Li, Z., Ge, J. and Yang, G., 2021. Influence of no-tillage and precipitation pulse on continuous soil respiration of summer maize affected by soil water in the North China Plain. Science of The Total Environment. 766, 144384.

Du, Y., Wang, Y.P., Hui, D., Su, F. and Yan, J., 2023. Significant effects of precipitation frequency on soil respiration and its components—A global synthesis. Global Change Biology. 29, 1188-1205.

Ebeling, A., Oerter, E., Valley, J.W. and Amundson, R., 2016. Relict soil evidence for profound quaternary aridification of the Atacama Desert, Chile. Geoderma. 267, 196-206.

Eddudóttir, S.D., Erlendsson, E. and Gísladóttir, G., 2020. Landscape change in the Icelandic highland: A long-term record of the impacts of land use, climate and volcanism. Quaternary Science Reviews. 240, 106363.

Eiler, J.M. and Schauble, E., 2004. 18O13C16O in Earth's atmosphere. Geochimica et Cosmochimica Acta. 68, 4767-4777.

Eiler, J.M., 2007. “Clumped-isotope” geochemistry—The study of naturally-occurring, multiply-substituted isotopologues. Earth and planetary science letters. 262, 309-327.

Eiler, J.M., 2011. Paleoclimate reconstruction using carbonate clumped isotope thermometry. Quaternary Science Reviews. 30, 3575-3588.

Eswaran, H., Sys, C., 1979. Argillic horizon formation in low activity clay soils, formation and significance to classification Pedologie. 29, 175-190

Fedoroff, N., Courty, M.A. and Guo, Z., 2010. Palaeosoils and relict soils. In Interpretation of micromorphological features of soils and regoliths. Elsevier. 623-662.

Feng, Z.Q., Jia, C.Z., Xie, X.N., Zhang, S., Feng, Z.H., and Cross, T.A., 2010. Tectonostratigraphic units and stratigraphic sequences of the non-marine Songliao basin, northeast China. Basin Research. 22, 79–95.

Feng, Z., Wang, C., Graham, S., Koeberl, C., Dong, H., Huang, Y., Gao, Y., 2013. Continental Scientific Drilling Project of Cretaceous Songliao Basin: Scientific objectives and drilling technology. Paleogeogr. Paleoclimatol. Paleoecol. 385, 6–16

Fesharaki, O., Garcı´a-Romero, E., Cuevas-Gonza´lez, J., and Lo´ pez-Martı´nez, N., 2007. Clay mineral genesis and chemical evolution in the Miocene sediments of Somosaguas, Madrid Basin, Spain. Clay Minerals. 42, 187-201.

Fiebig, J., Bajnai, D., Löffler, N., Methner, K., Krsnik, E., Mulch, A. and Hofmann, S., 2019. Combined high-precisionΔ 48 andΔ 47 analysis of carbonates. Chemical Geology. 522, 186-191.

Franke, D. and Ehrmann, W., 2010. Neogene clay mineral assemblages in the AND-2A drill core (McMurdo Sound, Antarctica) and their implications for environmental change. Palaeogeography, Palaeoclimatology, Palaeoecology. 286, 55-65.

Gagnon, C.A., Butler, K.L., Gaviria, E., Terrazas, A., Gao, A., Bhattacharya, T., Boutt, D.F., Munk, L.A. and Ibarra, D.E., 2023. Paleoclimate controls on lithium enrichment in Great Basin Pliocene− Pleistocene lacustrine clays. Geological Society of America Bulletin.

Gallagher, T.M. and Sheldon, N.D., 2013. A new paleothermometer for forest paleosols and its implications for Cenozoic climate. Geology. 41, 647-650.

Gao, Y., Wang, C., Liu, Z., Zhao, B., and Zhang, X. (2013) Clay mineralogy of the middle Mingshui Formation (upper Campanian to lower Maastrichtian) from the SK-1n bore-hole in the Songliao Basin, NE China: Implications for palaeoclimate and provenance. Palaeogeography, Palaeoclimatology, Palaeoecology. 385, 162-170.

[a]Gao, Yuan, Daniel E. Ibarra, Chengshan Wang, Jeremy K. Caves, C. Page Chamberlain, Stephan A. Graham, and Huaichun Wu., 2015. "Mid-latitude terrestrial climate of East Asia linked to global climate in the Late Cretaceous." Geology. 43, 287-290.

Gao, Y., Ibarra, D.E., Caves, J.K., Wang, C., Chamberlain, P., Graham, S.A., Wu, H., 2016. Mid-latitude terrestrial climate of East Asia linked to global climate in the Late Cretaceous: REPLY. Geology. 44, 379.

[b]Gao, Y., Wang, C., Liu, Z., Du, X. and Ibarra, D.E., 2015. Diagenetic and paleoenvironmental controls on Late Cretaceous clay minerals in the Songliao Basin, Northeast China. Clays and Clay Minerals. 63, 469-484.

[a]Gao, Y., Ibarra, D.E., Rugenstein, J.K.C., Chen, J., Kukla, T., Methner, K., Gao, Y., Huang, H., Lin, Z., Zhang, L. and Xi, D., 2021. Terrestrial climate in mid-latitude East Asia from the latest Cretaceous to the earliest Paleogene: A multiproxy record from the Songliao Basin in northeastern China. Earth-Science Reviews. 216, 103572.

[b]Gao, Y., Gao, Y., Ibarra, D.E., Du, X., Dong, T., Liu, Z. and Wang, C., 2021. Clay mineralogical evidence for mid-latitude terrestrial climate change from the latest Cretaceous through the earliest Paleogene in the Songliao Basin, NE China. Cretaceous Research.124, 104827.

Gaumont-Guay, D., Black, T.A., Griffis, T.J., Barr, A.G., Jassal, R.S. and Nesic, Z., 2006. Interpreting the dependence of soil respiration on soil temperature and water content in a boreal aspen stand. Agricultural and Forest Meteorology. 140, 220-235.

Gasse, F., Chalié, F., Vincens, A., Williams, M.A. and Williamson, D., 2008. Climatic patterns in equatorial and southern Africa from 30,000 to 10,000 years ago reconstructed from terrestrial and near-shore proxy data. Quaternary Science Reviews. 27, 2316-2340.

Ghosh, P., Adkins, J., Affek, H., Balta, B., Guo, W., Schauble, E.A., Schrag, D. and Eiler, J.M., 2006. 13C–18O bonds in carbonate minerals: A new kind of paleothermometer. Geochimica et Cosmochimica Acta. 70, 1439-1456.

Ghosh, P., Eiler, J., Campana, S.E. and Feeney, R.F., 2007. Calibration of the carbonate 'clumped isotope' paleothermometer for otoliths. Geochimica et Cosmochimica Acta. 71, 2736-2744.

Gillson, L., Waldron, S. and Willis, K.J., 2004. Interpretation of soil δ13C as an indicator of vegetation change in African savannas. Journal of Vegetation Science. 15, 339-350.

Grasby, S.E., Them II, T.R., Chen, Z., Yin, R. and Ardakani, O.H., 2019. Mercury as a proxy for volcanic emissions in the geologic record. Earth-Science Reviews. 196, 102880.

Gu, X., Zhang, L., Yin, R., Grasby, S.E., Yao, H., Tan, J. and Wang, C., 2022. Deccan volcanic activity and its links to the end-Cretaceous extinction in northern China. Global and Planetary Change. 210, 103772.

Hamer, J.M.M., Sheldon, N.D., Nichols, G.J. and Collinson, M.E., 2007. Late Oligocene–early Miocene paleosols of distal fluvial systems, Ebro Basin, Spain. Palaeogeography, Palaeoclimatology, Palaeoecology. 247, 220-235.

Hartley, A.J., May, G., 1998. Miocene gypcretes in the Calama Basin, northern Chile. Sedimentology. 45, 351–364.

Havinga, A.J., 1967. Palynology and pollen preservation. Review of Palaeobotany and Palynology. 2, 81-98.

Havinga, A.J., 1971. An experimental investigation into the decay of pollen and spores in various soil types. In Sporopollenin Academic Press. 446-479.

He, H., Deng, C., Wang, P., Pan, Y., Zhu, R., 2012. Toward age determination of the termination of the Cretaceous Normal Superchron. Geochem. Geophys. Geosyst. 13.

Henkes, G.A., Passey, B.H., Wanamaker Jr, A.D., Grossman, E.L., Ambrose Jr, W.G. and Carroll, M.L., 2013. Carbonate clumped isotope compositions of modern marine mollusk and brachiopod shells. Geochimica et Cosmochimica Acta. 106, 307-325.

Hernandez Nava, A., Black, B.A., Gibson, S.A., Bodnar, R.J., Renne, P.R. and Vanderkluysen, L., 2021. Reconciling early Deccan Traps CO2 outgassing and pre-KPB global climate. Proceedings of the National Academy of Sciences. 118, 2007797118.

Cenozoic CO2 Proxy Integration Project (CenCO2PIP) Consortium*†, Hönisch, B., Royer, D.L., Breecker, D.O., Polissar, P.J., Bowen, G.J., Henehan, M.J., Cui, Y., Steinthorsdottir, M., McElwain, J.C. and Kohn, M.J., 2023. Toward a Cenozoic history of atmospheric CO2. Science. 382, 5177.

Hu, H. R., and W. H. Qian, 2007: Identification of the northernmost boundary of East Asia summer monsoon. Progress in Natural Sciences. 17, 812–820.

Huang, B.W., 1959. Draft of the complex physical geographical division of China. Chinese Science Bulletin of China. 18, 594-602.

Huber, B.T., Hodell, D.A. and Hamilton, C.P., 1995. Middle–Late Cretaceous climate of the southern high latitudes: stable isotopic evidence for minimal equator-to-pole thermal gradients. Geological Society of America Bulletin. 107, 1164-1191.

Huber, B.T., Norris, R.D. and MacLeod, K.G., 2002. Deep-sea paleotemperature record of extreme warmth during the Cretaceous. Geology. 30, 123-126.

Huber, B.T., MacLeod, K.G., Watkins, D.K. and Coffin, M.F., 2018. The rise and fall of the Cretaceous Hot Greenhouse climate. Global and Planetary Change. 167, 1-23.

Hull, P.M., Bornemann, A., Penman, D.E., Henehan, M.J., Norris, R.D., Wilson, P.A., Blum, P., Alegret, L., Batenburg, S.J., Bown, P.R. and Bralower, T.J., 2020. On impact and volcanism across the Cretaceous-Paleogene boundary. Science. 367, 266-272.

Huntington, K.W., Eiler, J.M., Affek, H.P., Guo, W., Bonifacie, M., Yeung, L.Y., Thiagarajan, N., Passey, B., Tripati, A., Daëron, M. and Came, R., 2009. Methods and limitations of 'clumped'CO2 isotope (Δ47) analysis by gas-source isotope ratio mass spectrometry. Journal of Mass Spectrometry. 44, 1318-1329.

Huntington, K.W., Wernicke, B.P. and Eiler, J.M., 2010. Influence of climate change and uplift on Colorado Plateau paleotemperatures from carbonate clumped isotope thermometry. Tectonics, 29.

Huntington, K.W. and Lechler, A.R., 2015. Carbonate clumped isotope thermometry in continental tectonics. Tectonophysics. 647, 1-20.

Huntington, K.W. and Petersen, S.V., 2023. Frontiers of Carbonate Clumped Isotope Thermometry. Annual Review of Earth and Planetary Sciences. 51, 611-641.

Huyghe, D., Daëron, M., de Rafelis, M., Blamart, D., Sébilo, M., Paulet, Y.M. and Lartaud, F., 2022. Clumped isotopes in modern marine bivalves. Geochimica et Cosmochimica Acta. 316, 41-58.

Ibarra, D.E., Dai, J., Gao, Y., Lang, X., Duan, P., Gao, Z., Chen, J., Methner, K., Sha, L., Tong, H. and Han, X., 2023. High-elevation Tibetan Plateau before India–Eurasia collision recorded by triple oxygen isotopes. Nature Geoscience. 16, 810-815.

Jautzy, J.J., Savard, M.M., Dhillon, R.S., Bernasconi, S.M. and Smirnoff, A., 2020. Clumped isotope temperature calibration for calcite: Bridging theory and experimentation. Geochemical Perspectives Letters. 14, 36-41.

John, C. M., and Bowen, D., 2016. Community software for challenging isotope analysis: First alications of 'Easotope' to clumped isotopes. Rapid Commun. Mass Spectrom. 30, 2285–2300.

Johnson, D.W., Todd Jr, D.E., Trettin, C.F. and Sedinger, J.S., 2007. Soil carbon and nitrogen changes in forests of Walker Branch watershed, 1972 to 2004. Soil Science Society of America Journal. 71, 1639-1646.

Keller, G., Mateo, P., Monkenbusch, J., Thibault, N., Punekar, J., Spangenberg, J.E., Abramovich, S., Ashckenazi-Polivoda, S., Schoene, B., Eddy, M.P. and Samperton, K.M., 2020. Mercury linked to Deccan Traps volcanism, climate change and the end-Cretaceous mass extinction. Global and Planetary Change. 194, 103312.

Kelson, J.R., Watford, D., Bataille, C., Huntington, K.W., Hyland, E. and Bowen, G.J., 2018. Warm terrestrial subtropics during the Paleocene and Eocene: Carbonate clumped isotope (Δ47) evidence from the Tornillo Basin, Texas (USA). Paleoceanography and Paleoclimatology. 33, 1230-1249.

Kelson, J.R., Huntington, K.W., Breecker, D.O., Burgener, L.K., Gallagher, T.M., Hoke, G.D. and Petersen, S.V., 2020. A proxy for all seasons? A synthesis of clumped isotope data from Holocene soil carbonates. Quaternary Science Reviews. 234, 106259.

Khormali, F., Shahriari, A., Ghafarpour, A., Kehl, M., Lehndorff, E. and Frechen, M., 2020. Pedogenic carbonates archive modern and past precipitation change–A transect study from soils and loess-paleosol sequences from northern Iran. Quaternary International. 552, 79-90.

Kim, S.T. and O'Neil, J.R., 1997. Equilibrium and nonequilibrium oxygen isotope effects in synthetic carbonates. Geochimica et cosmochimica acta. 61, 3461-3475.

Kohfeld, K.E., Graham, R.M., De Boer, A.M., Sime, L.C., Wolff, E.W., Le Quéré, C. and Bo, L., 2013. Southern Hemisphere westerly wind changes during the Last Glacial Maximum: paleo-data synthesis. Quaternary Science Reviews. 68, 76-95.

Kohn, M.J., 2010, Carbon isotope compositions of terrestrial C3 plants as indicators of (paleo)ecology and (paleo)climate: Proceedings of the National Academy of Sciences of the United States of America. 107, 19,691–19,695.

Kong, Yanlong, Ke Wang, Jie Li, and Zhonghe Pang. 2019. "Stable Isotopes of Precipitation in China: A Consideration of Moisture Sources" Water. 11, 1239.

Kukla, T., Rugenstein, J.K.C., Ibarra, D.E., Winnick, M.J., Strömberg, C.A. and Chamberlain, C.P., 2022. Drier winters drove Cenozoic open habitat expansion in North America. AGU Advances. 3.

Li, L. Q., Keller, G., 1998. Abrupt deep-sea warming at the end of the Cretaceous. Geology. 26, 995-998.

Li, J. and Fang, X., 1999. Uplift of the Tibetan Plateau and environmental changes. Chinese science bulletin. 44, .2117-2124.

Li, J., Batten, D.J., Zhang, Y., 2011. Palynological record from a composite core through late Cretaceous–early Paleocene deposits in the Songliao Basin, Northeast China and its biostratigraphic implications. Cretaceous Research. 32, 1–12.

Li, X.F., Zhang, M.J., Ma, Q., Li, Y.J., Wang, S.J., and Wang, B.L., 2012, Characteristics of stable isotopes in precipitation over northeast China and its water vapor sources (in Chinese with English abstract): Environmental Sciences. 33, 2924–2931.

Li, J.; Pang, Z.; Kong, Y.; Zhou, M.; Huang, T. 2014. Spatial distributions of stable isotopic composition and deuterium excess in precipitation during the summer and winter seasons in China, Fresenius Environmental Bulletin. Fresenius Environ. Bull. 23, 2074–2085.

Li, X., Huang, Y., Zhang, Z. and Wang, C., 2022. Chemical weathering characteristics of the Late Cretaceous Nenjiang Formation from the Songliao Basin (Northeastern China) reveal prominent Milankovitch band variations. Palaeogeography, Palaeoclimatology, Palaeoecology. 601, 111130.

Licht, A., Dupont-Nivet, G., Meijer, N., Rugenstein, J.C., Schauer, A., Fiebig, J., Mulch, A., Hoorn, C., Barbolini, N. and Guo, Z., 2020. Decline of soil respiration in northeastern Tibet through the transition into the Oligocene icehouse. Palaeogeography, Palaeoclimatology, Palaeoecology. 560, 110016.

Linnert, C., Robinson, S.A., Lees, J.A., Bown, P.R., Pérez-Rodríguez, I., Petrizzo, M.R., Falzoni, F., Littler, K., Arz, J.A. and Russell, E.E., 2014. Evidence for global cooling in the Late Cretaceous. Nature communications. 5, 4194.

Liu, T. and Ding, Z., 1998. Chinese loess and the paleomonsoon. Annual review of earth and planetary sciences. 26, 111-145.

Liu, J.; Song, X.; Yuan, G.; Sun, X.; Yang, L., **2014.** Stable isotopic compositions of precipitation in China. Tellus. 66, 22567.

Lloyd, J. and Taylor, J.A., 1994. On the temperature dependence of soil respiration. Functional ecology. 315-323.

Luo, K.F., 1954. Draft of natural geography regionalization of China. Acta Geographica Sinica. 20, 379-394.

Luo, Y., Wan, S., Hui, D. and Wallace, L.L., 2001. Acclimatization of soil respiration to warming in a tall grass prairie. Nature. 413, 622-625.

Ma, M., He, M., Zhao, M., Peng, C. and Liu, X., 2021. Evolution of atmospheric circulation across the Cretaceous–Paleogene (K–Pg) boundary interval in low-latitude East Asia. Global and Planetary Change. 199, 103435.

Mack, G.H. and James, W.C., 1994. Paleoclimate and the global distribution of paleosols. The Journal of Geology. 102, 360-366.

Marbut, C. F., 1935. Atlas of American agriculture. III. Soils of the United States. Washington, D.C., Government Printing Office

McLennan, S.M., 1993. Weathering and global denudation. The Journal of Geology. 101, 295-303.

Meinicke, N., Reimi, M.A., Ravelo, A.C. and Meckler, A.N., 2021. Coupled Mg/Ca and clumped isotope measurements indicate lack of substantial mixed layer cooling in the Western Pacific Warm Pool during the last~ 5 million years. Paleoceanography and Paleoclimatology. 36.

Melillo, J.M., Steudler, P.A., Aber, J.D., Newkirk, K., Lux, H., Bowles, F.P., Catricala, C., Magill, A., Ahrens, T. and Morrisseau, S., 2002. Soil warming and carbon-cycle feedbacks to the climate system. Science. 298, 2173-2176.

Montañez, I.P., 2013, Modern soil system constraints on reconstructing deep-time atmospheric CO2 : Geochimica et Cosmochimica Acta. 101, 57– 75,

Mudelsee, M., Bickert, T., Lear, C.H. and Lohmann, G., 2014. Cenozoic climate changes: A review based on time series analysis of marine benthic δ18O records. Reviews of Geophysics. 52, 333-374.

Murray, R.W., Miller, D.J., and Kryc, K.A., 2000. Analysis of major and trace elements in rocks, sediments, and interstitial waters by inductively coupled plasma-atomic emission spectrometry (ICP-AES). ODP Tech. Note, 29

Myers, T.S., Tabor, N.J., Jacobs, L.L. and Mateus, O., 2012. Estimating soil pCO2 using paleosol carbonates: implications for the relationship between primary productivity and faunal richness in ancient terrestrial ecosystems. Paleobiology. 38, 585-604.

Myers, T.S., Tabor, N.J., Jacobs, L.L. and Bussert, R., 2016. Effects of different organic-matter sources on estimates of atmospheric and soil pCO2 using pedogenic carbonate. Journal of Sedimentary Research. 86, 800-812.

Nesbitt, H.W. and Young, G.M., 1984. Prediction of some weathering trends of plutonic and volcanic rocks based on thermodynamic and kinetic considerations. Geochimica et cosmochimica acta. 48, 1523-1534.

Niroumand Fard, F., Khashei Siuki, A., Hashemi, S.R. and Ghorbani, K., 2023. Evaluation of the effect of scenarios in the 6th report of IPCC on the prediction groundwater level using the non-linear model of the input-output time series. Environmental Monitoring and Assessment. 195, 1359.

Nordt, L., Atchley, S., Dworkin, S., 2003. Terrestrial evidence for two greenhouse events in the latest Cretaceous. GSA Today. 13, 4–9.

Norby, R.J., Wullschleger, S.D., Gunderson, C.A., Johnson, D.W. and Ceulemans, R., 1999. Tree responses to rising CO2 in field experiments: implications for the future forest. Plant, Cell & Environment. 22, 683-714.

O'Connor, L.K., 2023. Steady decline in mean annual air temperatures in the first 30 ky after the Cretaceous-Paleogene boundary: Geology.

Ohba, M. and Ueda, H., 2010. A GCM study on effects of continental drift on tropical climate at the early and late Cretaceous. Journal of the Meteorological Society of Japan. Ser. II, 88(6), pp.869-881.

Okusami, T.A., Rust, R.H. and Alao, A.O., 1997. Red soils of different origins from southwest Nigeria: characteristics, classification, and management considerations. Canadian journal of soil science. 77, 295-307.

Passey, B.H. and Henkes, G.A., 2012. Carbonate clumped isotope bond reordering and geospeedometry. Earth and Planetary Science Letters. 351, 223-236.

Peral, M., Daëron, M., Blamart, D., Bassinot, F., Dewilde, F., Smialkowski, N., Isguder, G., Bonnin, J., Jorissen, F., Kissel, C. and Michel, E., 2018. Updated calibration of the clumped isotope thermometer in planktonic and benthic foraminifera. Geochimica et Cosmochimica Acta. 239, 1-16.

Percival, L.M., Jenkyns, H.C., Mather, T.A., Dickson, A.J., Batenburg, S.J., Ruhl, M., Hesselbo, S.P., Barclay, R., Jarvis, I., Robinson, S.A. and Woelders, L., 2018. Does large

igneous province volcanism always perturb the mercury cycle? Comparing the records of Oceanic Anoxic Event 2 and the end-Cretaceous to other Mesozoic events. American Journal of Science. 318, 799-860.

Peters, N.A., Huntington, K.W. and Hoke, G.D., 2013. Hot or not? Impact of seasonally variable soil carbonate formation on paleotemperature and O-isotope records from clumped isotope thermometry. Earth and Planetary Science Letters. 361, 208-218.

Piao, S. and Wang, X., 2023. Biological systems under climate change: What do we learn from the IPCC AR6. Global Change Biology. 29, 5120-5121.

Prochnow, S.J., Nordt, L.C., Atchley, S.C. and Hudec, M.R., 2006. Multi-proxy paleosol evidence for middle and late Triassic climate trends in eastern Utah. Palaeogeography, Palaeoclimatology, Palaeoecology. 232, 53-72.

Polyakov, V.B., Horita, J., Cole, D.R., 2005. Isotopic self-exchange reactions of water: Evaluation of the rule of the geometric mean in liquid-vapor isotope partitioning. J. Phys. Chem. 109, 8642–8645.

Qing-Yu, J., Wen-Ying, Y., Li, Z., Ri-Hong, W., Yan-bing, X. and Ni-Na, C., 2019. Methane emissions from typical paddy fields in Liaohe Plain and Sanjiang Plain, Northeast China. Environmental Research Communications. 1, 011006.

Qu, H., Xi, D., Li, S., Colin, J.P., Huang, Q., Wan, X., 2014. Late Cretaceous–early Paleocene ostracod biostratigraphy of Scientific Drilling Sk1(N) in the Songliao Basin, Northeast China. J. Paleontol. 88, 786–798.

Quade, J., Cerling, T.E. and Bowman, J.R., 1989. Development of Asian monsoon revealed by marked ecological shift during the latest Miocene in northern Pakistan. Nature. 342, 163-166.

Quade, J., Garzione, C. and Eiler, J., 2007. Paleoelevation reconstruction using pedogenic carbonates. Reviews in Mineralogy and Geochemistry. 66, 53-87.

Quade, J., Eiler, J., Daeron, M. and Achyuthan, H., 2013. The clumped isotope geothermometer in soil and paleosol carbonate. Geochimica et Cosmochimica Acta. 105, 92-107.

Randriamarolaza, L.Y.A., Aguilar, E., Skrynyk, O., Vicente-Serrano, S.M. and Domínguez-Castro, F., 2022. Indices for daily temperature and precipitation in Madagascar, based on quality-controlled and homogenized data, 1950–2018. International Journal of Climatology. 42, 265-288.

Raymo, M.E. and Ruddiman, W.F., 1992. Tectonic forcing of late Cenozoic climate. Nature. 359, 117-122.

Retallack, G.J. and Mindszenty, A., 1994. Well preserved late Precambrian paleosols from northwest Scotland. Journal of Sedimentary Research. 64, 264-281.

Retallack, Gregory J., 1997, "Neogene expansion of the North American prairie." Palaios 12, 380-390.

Retallack, G.J. and Krull, E.S., 1999. Landscape ecological shift at the Permian-Triassic boundary in Antarctica. Australian Journal of Earth Sciences. 46, 785.

Retallack, G.J., 2000. Ordovician life on land and early Paleozoic global change. The Paleontological Society Papers. 6, 21-46.

Retallack, G.J., 2005, Pedogenic carbonate proxies for amount and seasonality of precipitation in paleosols: Geology. 33, 333.

Rosenzweig, C. and Hillel, D., 1995. Potential impacts of climate change on agriculture and food supply. Consequences. 1, 23-32.

Rugenstein, J.K.C. and Chamberlain, C.P., 2018. The evolution of hydroclimate in Asia over the Cenozoic: A stable-isotope perspective. Earth-Science Reviews. 185, 1129-1156.

Rustad, L.E.J.L., Campbell, J., Marion, G., Norby, R., Mitchell, M., Hartley, A., Cornelissen, J., Gurevitch, J. and Gcte-News, 2001. A meta-analysis of the response of soil respiration, net nitrogen mineralization, and aboveground plant growth to experimental ecosystem warming. Oecologia. 126, 543-562.

Saxe H, Ellsworth DS, Heath J. 1998. Tree and forest functioning in an enriched CO2 atmosphere. New Phytologist 139(3): 395-436.

Sayyed, M.R.G. and Hundekari, S.M., 2006. Preliminary comparison of ancient bole beds and modern soils developed upon the Deccan volcanic basalts around Pune (India): Potential for palaeoenvironmental reconstruction. Quaternary International. 156, 189-199.

Schoene, B., Eddy, M.P., Samperton, K.M., Keller, C.B., Keller, G., Adatte, T. and Khadri, S.F., 2019. U-Pb constraints on pulsed eruption of the Deccan Traps across the end-Cretaceous mass extinction. Science. 363, 862-866.

Schoene, B., Eddy, M.P., Keller, C.B. and Samperton, K.M., 2020. An evaluation of Deccan Traps eruption rates using geochronologic data. Geochronology Discussions. 2020, 1-25.

Senel, C.B., Kaskes, P., Temel, O., Vellekoop, J., Goderis, S., DePalma, R., Prins, M.A., Claeys, P. and Karatekin, Ö., 2023. Chicxulub impact winter sustained by fine silicate dust. Nature Geoscience. 1-8.

Sharp, Z. D., & Wostbrock, J. A. (2021). Standardization for the triple oxygen isotope system: Waters, silicates, carbonates, air, and sulfates. Reviews in Mineralogy and Geochemistry. 86, 179-196.

Shaw, J.N., West, L.T., Bosch, D.D., Truman, C.C. and Leigh, D.S., 2004. Parent material influence on soil distribution and genesis in a Paleudult and Kandiudult complex, southeastern USA. Catena. 57, 157-174.

Sheldon, N.D., Retallack, G.J. and Tanaka, S., 2002. Geochemical climofunctions from North American soils and alication to paleosols across the Eocene-Oligocene boundary in Oregon. The Journal of geology. 110, 687-696.

Sheldon, N.D., 2006. Using paleosols of the Picture Gorge Basalt to reconstruct the middle Miocene climatic optimum. PaleoBios. 26, 27–36.

Sheldon, N.D. and Tabor, N.J., 2009. Quantitative paleoenvironmental and paleoclimatic reconstruction using paleosols. Earth-science reviews. 95, 1-52.

Shen, J., Feng, Q., Algeo, T.J., Liu, J., Zhou, C., Wei, W., Liu, J., Them II, T.R., Gill, B.C. and Chen, J., 2020. Sedimentary host phases of mercury (Hg) and implications for use of Hg as a volcanic proxy. Earth and Planetary Science Letters. 543, 116333.

Soil Survey Staff. 2022. Keys to Soil Taxonomy, 13th ed. USDA-Natural Resources Conservation Service.

Song, Z., Qin, Y., George, S.C., Wang, L., Guo, J., and Feng, Z., 2013, A biomarker study of depositional paleoenvironments and source inputs for the massive formation of Uer Cretaceous lacustrine source rocks in the Songliao Basin, China: Palaeogeography, Palaeoclimatology, Palaeoecology. 385, 137-151.

Spencer, C. and Kim, S.T., 2015. Carbonate clumped isotope paleothermometry: a review of recent advances in CO 2 gas evolution, purification, measurement and standardization techniques. Geosciences Journal. 19, 357-374.

Sprain, C.J., Renne, P.R., Wilson, G.P., Clemens, W.A., 2015. High-resolution chronostratigraphy of the terrestrial Cretaceous-Paleogene transition and recovery interval in the Hell Creek region. Montana. Geol. Soc. Am. Bull. 127, 393–409.

Sprain, C.J., Renne, P.R., Vanderkluysen, L., Pande, K., Self, S. and Mittal, T., 2019. The eruptive tempo of Deccan volcanism in relation to the Cretaceous-Paleogene boundary. Science. 363, 866-870.

Stiles, C.A., Stensvold, K.A., 2008. Loess contribution to soils forming on dolostone in the Driftless Area of Wisconsin. Soil Science Survey of America Journal. 72, 650–659.

Strömgren, M., 2001. Soil-surface CO2 flux and growth in a boreal Norway spruce stand. 220.

Tabor, N.J. and Myers, T.S., 2015. Paleosols as indicators of paleoenvironment and paleoclimate. Annual Review of Earth and Planetary Sciences. 43, 333-361.

Tadross, M., Randriamarolaza, L., Rabefitia, Z. and Zheng, K.Y., 2008. Climate change in Madagascar; recent past and future. World Bank, Washington, DC. 18, 1771-1790.

Tang, X., Sun, G. and Qian, W.H., 2007. A Study of Boundary Belt for East Asian Summer Monsoon. China Meteorological Press. 42–48.

Them II, T.R., Jagoe, C.H., Caruthers, A.H., Gill, B.C., Grasby, S.E., Gröcke, D.R., Yin, R. and Owens, J.D., 2019. Terrestrial sources as the primary delivery mechanism of mercury to the oceans across the Toarcian Oceanic Anoxic Event (Early Jurassic). Earth and Planetary Science Letters. 507, 62-72.

Terry Jr, D.O., 2001. Paleopedology of the Chadron Formation of Northwestern Nebraska: implications for paleoclimatic change in the North American midcontinent across the Eocene–Oligocene boundary. Palaeogeography, Palaeoclimatology, Palaeoecology. 168, 1-38.

Thibodeau, A.M., Bergquist, B.A., 2017. Do mercury isotopes record the signature of massive volcanism in marine sedimentary records?. Geology. 45, 95-96.

Tian, L., Masson-Delmotte, V., Stievenard, M., Yao, T. and Jouzel, J., 2001. Tibetan Plateau summer monsoon northward extent revealed by measurements of water stable isotopes. Journal of Geophysical Research: Atmospheres. 106, 28081-28088.

Tile, B.J. and Pagani, M., 2007. The early origins of terrestrial C4 photosynthesis. Annu. Rev. Earth Planet. Sci. 35, 435-461.

Tile, B.J., Meyers, S.R., and Pagani, M., 2010, Carbon isotope ratio of Cenozoic CO2: A comparative evaluation of available geochemical proxies: Paleoceanography. 25, PA3202.

Thornburg, J.D., Miller, K.G., Browning, J.V. and Wright, J.D., 2019. Mid-Cretaceous paleopedology and landscape reconstruction of the Mid-Atlantic US Coastal Plain. Journal of Sedimentary Research, 89, 253-272.

Tobin, T.S., Wilson, G.P., Eiler, J.M., Hartman, J.H., 2014. Environmental change across a terrestrial Cretaceous-Paleogene boundary section in eastern Montana, USA, constrained by carbonate clumped isotope paleothermometry. Geology. 42, 351–354

Toggweiler, J.R., 2009. Shifting westerlies. Science. 323, 1434-1435.

Trakoonyingcharoen, P., Kheoruenromne, I., Suddhiprakarn, A. and Gilkes, R.J., 2006. Properties of iron oxides in red Oxisols and red Ultisols as affected by rainfall and soil parent material. Soil Research. 44, 63-70.

Tucker, R.T., Crowley, J.L., Mohr, M.T., Renaut, R.K., Makovicky, P.J. and Zanno, L.E., 2023. Exceptional age constraint on a fossiliferous sedimentary succession preceding the Cretaceous Thermal Maximum. Geology. 51, 962-967.

Újvári, G., Kele, S., Bernasconi, S.M., Haszpra, L., Novothny, Á. and Bradák, B., 2019. Clumped isotope paleotemperatures from MIS 5 soil carbonates in southern Hungary. Palaeogeography, Palaeoclimatology, Palaeoecology. 518, 72-81.

Urey, H.C., 1947. The thermodynamic properties of isotopic substances. Journal of the Chemical Society (Resumed). 562-581.

Wan, X., Zhao, J., Scott, R.W., Wang, P., Feng, Z., Huang, Q., Xi, D., 2013. Late Cretaceous stratigraphy, Songliao Basin, NE China: SK1 cores. Paleogeogr. Paleoclimatol. Paleoecol. 385, 31–43.

Wang, Z., Schauble, E.A. and Eiler, J.M., 2004. Equilibrium thermodynamics of multiply substituted isotopologues of molecular gases. Geochimica et Cosmochimica Acta. 68, 4779-4797.

Wang, C., Feng, Z., Zhang, L., Huang, Y., Cao, K., Wang, P. and Zhao, B., 2013. Cretaceous paleogeography and paleoclimate and the setting of SKI borehole sites in Songliao Basin, northeast China. Palaeogeography, Palaeoclimatology, Palaeoecology. 385, 17-30.

Wang, Y., Huang, C., Sun, B., Quan, C., Wu, J. and Lin, Z., 2014. Paleo-CO2 variation trends and the Cretaceous greenhouse climate. Earth-Science Reviews. 129, 136-147.

Wang, G., Cheng, R., Wang, P., Gao, Y., Wang, C., Ren, Y., Huang, Q., 2015. High resolution continuous sedimentary records of Uer Cretaceous obtained from the continental drilling (SK-1) borehole in Songliao Basin: Sifangtai and Mingshui Formations. Geosci. Front. 6, 895–912.

Wang, C., Gao, Y., Ibarra, D. E., Wu, H., Wang, P., 2021. An unbroken record of climate during the age of dinosaurs. Eos. 102.

Westerhold, T. and Röhl, U., 2009. High resolution cyclostratigraphy of the early Eocene–new insights into the origin of the Cenozoic cooling trend. Climate of the Past. 5, 309-327.

Westerhold, T., Röhl, U., Donner, B., McCarren, H. K., Zachos, J. C., 2011. A complete high-resolution Paleocene benthic stable isotope record for the central Pacific (ODP Site 1209). Paleoceanography. 26, PA2216.

Wilf, P., Johnson, K.R., Huber, B.T., 2003. Correlated terrestrial and marine evidence for global climate changes before mass extinction at the Cretaceous-Paleogene boundary. Proc. Natl. Acad. Sci. U. S. A. 100, 599–604.

Wilson, M.D. and Pittman, E.D., 1977. Authigenic clays in sandstones; recognition and influence on reservoir properties and paleoenvironmental analysis. Journal of Sedimentary Research. 47, 3-31.

Woelders, L., Vellekoop, J., Weltje, G.J., de Nooijer, L., Reichart, G.J., Peterse, F., Claeys, P. and Speijer, R.P., 2018. Robust multi-proxy data integration, using late Cretaceous paleotemperature records as a case study. Earth and Planetary Science Letters. 500, 215-224.

Wu, H., Zhang, S., Hinnov, L.A., Jiang, G., Yang, T., Li, H., Wan, X., Wang, C., 2014. Cyclostratigraphy and orbital tuning of the terrestrial uer Santonian–lower Danian in Songliao Basin. northeastern China. Earth Planet. Sci. Lett. 407, 82–95.

Vellekoop, J., Sluijs, A., Smit, J., Schouten, S., Weijers, J.W., Sinninghe Damsté, J.S. and Brinkhuis, H., 2014. Rapid short-term cooling following the Chicxulub impact at the Cretaceous–Paleogene boundary. Proceedings of the National Academy of Sciences. 111, 7537-7541.

Vellekoop, J., Esmeray-Senlet, S., Miller, K.G., Browning, J.V., Sluijs, A., van de Schootbrugge, B., Damsté, J.S.S. and Brinkhuis, H., 2016. Evidence for Cretaceous-Paleogene boundary bolide "impact winter" conditions from New Jersey, USA. Geology. 44, 619-622.

Vinogradov, A.P., 1959. Geochemistry of isotopes. International Geology Review. 1, 1-13.

Yan, T., Song, H., Wang, Z., Teramoto, M., Wang, J., Liang, N., Ma, C., Sun, Z., Xi, Y., Li, L. and Peng, S., 2019. Temperature sensitivity of soil respiration across multiple time scales in a temperate plantation forest. Science of the Total Environment. 688, 479-485.

Yang, S., Zhang, M., Wang, S., Liu, Y., Qiang, F. and Qu, D., 2017. Interannual trends in stable oxygen isotope composition in precipitation of China during 1979–2007: Spatial incoherence. Quaternary International. 454, 25-37.

Yang, H., Huang, Y., Ma, C., Zhang, Z. and Wang, C., 2020. Recognition of Milankovitch cycles in XRF core-scanning records of the Late Cretaceous Nenjiang Formation from the Songliao Basin (northeastern China) and their paleoclimate implications. Journal of Asian Earth Sciences. 194, 104183.

Yin, Y., Zhang, L., Gu, X., Yin, R., Wen, Y., Jin, T. and Wang, C., 2023. High terrestrial temperature in the low-latitude Nanxiong Basin during the Cretaceous-Paleogene boundary interval. Palaeogeography, Palaeoclimatology, Palaeoecology. 617, 111489.

Young, E.D., Manning, C.E., Schauble, E.A., Shahar, A., Macris, C.A., Lazar, C. and Jordan, M., 2015. High-temperature equilibrium isotope fractionation of non-traditional stable isotopes: Experiments, theory, and applications. Chemical Geology. 395, 176-195.

Xue, Z., Liu, X., Sawut, M., Liu, J., Zhao, X., Xing, L., Wang, R., Luo, X., Wang, C., Zhao, H. and Wang, Y., 2023. The spatial and temporal variability and influence factor analysis of soil erosion in a grass farming area: a case study in central China. Soil Research. 62.

Zachos, J., Pagani, M., Sloan, L., Thomas, E. and Billups, K., 2001. Trends, rhythms, and aberrations in global climate 65 Ma to present. Science. 292, 686-693.

Zhang, F.-Q., Dilek, Y., Chen, H.-L., Yang, S.-F., Meng, Q.-A., 2017. Structural architecture and stratigraphic record of late Mesozoic sedimentary basins in NE China:

Tectonic archives of the Late Cretaceous continental margin evolution in East Asia. Earth-Sci. Rev. 171, 598–620.

Zhang, L., Wang, C., Wignall, P.B., Kluge, T., Wan, X., Wang, Q. and Gao, Y., 2018. Deccan volcanism caused coupled pCO2 and terrestrial temperature rises, and pre-impact extinctions in northern China. Geology. 46, 271-274.

Zhang, Z., Li, Y., Williams, R.A., Chen, Y., Peng, R., Liu, X., Qi, Y. and Wang, Z., 2023. Responses of soil respiration and its sensitivities to temperature and precipitation: A meta-analysis. Ecological Informatics. 102057.

Zhou, X., Talley, M. and Luo, Y., 2009. Biomass, litter, and soil respiration along a precipitation gradient in southern Great Plains, USA. Ecosystems. 12, 1369-1380.

Appendix I. Data Tables

Table 1. Carbon and Oxygen Isotopic Data Produced Using IBEX Carbonate Peripheral

Sample ID	Age (Ma)	%$CaCO_3$	Depth (m)	Previously Published δ13C/δ18	δ13C (‰)	δ18O (‰)	δ18Opw (‰)	SE (+)	SE (-)	Temp (℃)	SE (+)	SE (-)
97-101-2.2	65.52	72.81	268.55	Gao et al., 2015	-9.16	21.88	-9.86	2.58	2.51	8.76	5.05	4.79
98-101-2.9	65.52	34.72	269.25	Gao et al., 2015	-8.76	22.74	-6.26	0.66	0.65	21.62	1.63	1.60
112-105-0.2	65.69	81.05	287.11	Gao et al., 2015	-9.67	21.10	-8.77	0.25	0.25	17.24	0.23	0.23
115-106-4.4	65.73	80.43	292.06	Gao et al., 2015	-9.11	20.05	-9.01	0.54	0.54	20.97	1.32	1.30
118-106-5.2	65.74	68.31	292.85	Gao et al., 2015	-7.91	19.79	-11.65	1.15	1.14	9.81	2.20	2.15
120-107-1.2	65.75	73.58	294.69	Gao et al., 2015	-8.84	21.56	-6.50	0.89	0.88	25.18	3.20	3.10
122-107-3.45	65.78	78.3	296.94	Gao et al., 2015	-8.99	22.11	-6.94	0.19	0.19	21.29	0.09	0.09
122-107-3.65	65.78	84.6	297.14	Gao et al., 2015	-9.05	22.03	-6.47	0.66	0.53	23.94	1.45	1.43
123-107-4.1	65.78	90.83	297.59	Gao et al., 2015	-9.29	21.88	-9.99	1.41	1.39	8.19	2.68	2.61
124-107-5.45	65.80	76.85	298.94	Gao et al., 2015	-8.09	22.88	-4.39	0.80	0.56	30.28	1.67	1.64
126-108-0.3	65.82	79.02	300.58	Gao et al., 2015	-7.88	22.18	-6.24	0.64	0.53	24.39	1.61	1.58
127-2	65.82	58.52	301.38	-	-7.49	21.97	-6.87	0.76	0.75	22.28	2.01	1.97
128-2	65.84	71.49	302.88	-	-8.09	21.64	-8.47	0.47	0.47	16.20	0.78	0.77
132-109-3.8	65.88	77.33	307.05	Gao et al., 2015	-9.39	21.44	-6.74	1.02	0.83	25.52	2.53	2.47
135-110-2.5	65.91	74.56	309.76	Gao et al., 2015	-8.03	22.12	-7.13	0.59	0.59	20.32	1.46	1.44
135-110-1	65.92	66.85	310.51	Gao et al., 2015	-8.11	22.51	-4.91	0.50	0.50	29.45	1.36	1.34
140-111-1.15	65.96	71.73	314.68	Gao et al., 2015	-6.98	22.03	-5.52	0.93	0.92	28.75	0.25	0.25
141-111-2.4	65.98	65.54	315.93	Gao et al., 2015	-6.63	21.88	-7.10	0.56	0.56	21.62	0.97	0.96
144-112-0.5	66.02	9.82	319.76	-	-7.09	28.52	1.39	0.33	0.32	31.78	0.90	0.89
144-112-2.5	66.05	7.26	321.76	-	-7.30	20.53	-5.29	0.69	0.68	37.56	2.43	2.38
147-112-3.8	66.06	10.24	323.06	-	-7.54	19.73	-8.92	0.86	0.86	22.94	1.74	1.71
149-113-0.1	66.09	17.34	325.54	-	-7.24	19.93	-8.00	1.04	1.03	26.54	2.43	2.38

150-113-1.2	66.10	9.66	326.64	-	-7.44	19.65	-6.02	1.55	1.51	37.31	3.62	3.50
151-113-2	66.11	7.36	327.44	-	-7.10	20.19	-7.07	0.65	0.65	24.95	3.42	3.31
152-114-0.5	66.12	8.18	328.24	-	-6.38	20.84	-8.00	0.51	0.50	22.17	2.84	2.76
153-115-0.3	66.14	8.13	329.62	-	-7.22	20.07	-8.13	2.12	2.06	25.18	5.52	5.23
154-116-0.3	66.15	8.46	330.16	-	-7.44	19.79	-8.40	0.32	0.32	25.18	0.49	0.49
155-3	66.16	5.82	331.21	-	-7.44	20.62	-7.71	2.39	2.31	24.61	6.40	6.01
155-116-1.3	66.16	7.2	331.31	-	-7.51	20.58	-8.04	1.25	1.23	23.16	3.06	2.97
155-2	66.16	7.59	331.51	-	-7.48	19.25	-9.52	2.59	2.55	19.67	4.39	4.20
156-116-2.3	66.17	5.38	332.31	-	-7.93	20.64	-6.55	19.11	21.05	30.40	4.30	4.11
156-2	66.18	5.12	332.61	-	-7.86	20.21	-8.70	0.87	0.86	21.73	2.10	2.05
157-116-3.3	66.19	4.82	333.31	-	-6.79	19.96	-7.11	1.87	1.83	30.88	4.62	4.42
157-1	66.19	8.26	333.56	-	-7.54	19.42	-9.42	1.57	1.53	21.95	4.46	4.27
159-118-1.6	66.22	60.25	335.87	-	-9.01	22.12	-4.33	1.24	1.21	34.42	3.52	3.40
159-118-1.7	66.22	70.85	335.97	Gao et al., 2015	-9.09	21.21	-7.00	0.38	0.38	25.29	0.90	0.89
160-118-2.5	66.23	5.71	336.77	Gao et al., 2015	-8.29	21.73	-5.65	1.45	1.42	28.63	3.51	3.39
161-3	66.24	8.34	337.32	-	-8.21	21.14	-10.26	1.63	0.12	10.20	1.62	1.59

*Long-term running Standard Error for $\delta^{18}O$ and $\delta^{13}C$ is < 0.1‰

* (-) denotes new data produced from this study

Table 2. Traditional Isotope Data Produced using the Kiel IV Carbonate Peripheral

Sample ID	Age (Ma)	Depth (m)	δ13C (‰)	δ18O (‰)	%$CaCO_3$
125	65.81	300.29	-8.19	-8.78	38.10
126-3	65.81	300.38	-8.13	-9.08	38.46
126-2	65.82	300.73	-7.96	-8.71	46.01
126-1	65.82	301.08	-7.52	-8.93	27.32
127-2	65.82	301.38	-7.64	-8.78	58.52
127-1	65.83	301.68	-8.28	-9.84	9.35
128-2	65.84	302.88	-8.12	-8.94	71.49
128	65.84	303.03	-7.98	-8.76	38.06
132	65.88	307.15	-9.32	-8.67	11.08
142-1113.8	65.99	317.33	-6.78	-9.53	2.15
143-111-4.3	66.00	317.83	-6.99	-9.19	10.03
144-112-0.5	66.02	319.76	-7.44	-10.26	9.82
144-112-2.5	66.05	321.76	-7.45	-10.45	7.26
147-112-3.4	66.06	322.66	-7.23	-10.43	6.71
147-112-3.8	66.06	323.06	-7.79	-10.29	10.24
148-112-4.2	66.07	323.46	-7.70	-11.18	6.73
148-112-4.7	66.07	323.96	-7.99	-11.39	9.07
149-113-0.1	66.09	325.54	-7.30	-10.68	17.34
150-113-0.8	66.10	326.24	-7.58	-11.80	15.66
150-113-1.2	66.10	326.64	-7.48	-10.81	9.66
151-113-2	66.11	327.44	-7.09	-10.35	7.36
152-114-0.5	66.12	328.24	-6.43	-9.71	8.18
152-114-1	66.13	328.74	-7.13	-10.96	9.37
153-115-0.3	66.14	329.62	-7.14	-10.46	8.13
154-116-0.3	66.15	330.16	-7.55	-10.24	8.46
155-3	66.16	331.21	-7.52	-10.11	5.82
155-116-1.3	66.16	331.31	-7.63	-10.26	7.20
155-2	66.16	331.51	-7.46	-10.38	7.59
156-116-2.3	66.17	332.31	-7.94	-10.29	5.38
156-1	66.17	332.41	-7.91	-10.49	3.62
156-2	66.18	332.61	-7.98	-10.72	5.12
156-3	66.18	332.81	-7.77	-10.20	3.25
157-2	66.18	332.81	-6.75	-10.17	3.34
156-4	66.18	332.91	-7.91	-10.20	3.58
157-1	66.19	333.56	-7.57	-10.75	8.26
157-116-3.3	66.19	333.31	-6.79	-10.52	4.82
159	66.22	335.97	-8.76	-9.46	3.99
159-118-1.6	66.22	335.87	-8.98	-8.92	60.25
160-118-2.1	66.23	336.37	-7.20	-9.45	5.86
160-118-2.5	66.23	336.77	-7.22	-9.47	5.71
161-3	66.24	337.32	-8.21	-8.80	8.34
161-2	66.24	337.57	-7.94	-8.62	5.79
161-1	66.24	337.77	-7.57	-8.96	2.81

162	66.30	340.65	-7.71	-9.26	2.88
166-2	66.30	342.27	-7.13	-11.32	2.77

Table 3. ICP-OES Major Elemental Concentrations

Age (Ma)	**Ca%**	**Mg%**	**Al%**	**Si%**	**Na%**	**Ba ppm**
67.49	4.24	1.80	7.97	22.37	0.44	117.44
67.25	6.17	2.38	10.04	25.16	0.50	179.53
66.60	7.57	2.07	9.81	29.19	0.67	547.48
66.30	5.04	2.20	9.69	26.76	0.53	148.95
66.24	8.64	2.27	9.26	23.41	0.34	140.33
66.24	9.18	2.54	9.75	20.78	0.27	112.29
66.24	5.45	2.17	9.04	24.28	0.40	102.67
66.23	6.04	2.45	9.99	25.01	0.61	137.37
66.23	6.04	2.45	9.99	25.01	0.61	137.37
66.18	5.86	3.13	11.14	23.57	0.26	112.33
66.18	7.18	3.10	11.19	23.05	0.25	113.42
66.17	6.58	3.37	11.80	25.06	0.39	116.67
66.07	5.40	2.35	10.04	27.84	0.78	162.44
66.06	5.97	1.75	9.39	31.72	0.77	166.68
66.05	5.85	1.85	9.70	30.26	0.65	180.25
66.02	6.25	1.36	7.92	26.60	0.79	169.06
66.00	4.31	0.89	6.23	25.37	1.34	531.75
65.96	1.37	0.82	6.20	26.97	1.33	547.85
65.93	3.04	1.56	8.29	30.19	1.06	414.46
65.93	2.23	1.29	7.21	27.33	1.12	342.66
65.91	3.12	1.93	7.85	22.72	0.49	295.54
65.89	27.78	16.35	68.88	188.70	3.73	2261.20
65.88	16.84	2.36	8.86	22.36	0.26	143.96
65.87	0.85	1.21	8.87	28.32	0.84	399.61
65.87	0.76	1.22	7.74	29.03	0.95	208.70
65.83	1.10	1.59	9.24	29.51	0.76	310.68
65.83	11.75	2.30	10.76	23.47	0.28	109.26
65.81	4.80	1.65	7.70	21.88	0.44	274.44
65.79	4.64	1.53	6.95	19.32	0.38	151.41
65.77	1.07	1.28	8.35	25.18	0.65	265.25
65.75	10.72	1.24	6.14	20.17	0.47	1502.54
65.73	1.20	1.63	9.04	25.24	0.51	185.15
65.71	1.04	1.31	9.06	25.40	0.56	370.80
65.70	1.01	1.36	9.23	25.66	0.51	359.11
65.64	1.00	1.14	8.09	24.61	0.71	417.94

65.63	0.91	0.57	4.31	16.12	0.60	156.49
65.58	1.07	1.48	8.55	29.69	0.68	414.42
65.53	2.56	1.08	7.26	24.40	0.54	687.72
65.48	0.53	0.54	5.50	23.82	1.00	285.42
65.42	1.04	1.50	8.66	28.39	0.56	375.44
65.37	8.00	9.95	75.98	263.10	4.07	1800.27
65.32	1.22	1.30	8.30	24.88	0.17	413.22

*Long term S.E. is < ± 5.000 %

Table 4. Results of four Soil Respiration modeling scenarios

Age (Ma)	Model 1	SE (+/-)	Model 2	SE (+/-)	Model 3	SE (+/-)	Model 4	SE (+/-)
65.52	1040.23	365.53	1140.25		1000.59		1093.54	446.96
65.69	1578.31	320.72	1140.34	279.71	1559.87	317.00	1130.02	241.90
65.73	975.51	1502.45	719.69	232.85	843.51	1681.70	640.19	284.90
65.74	828.18	1459.85	642.82	238.45	1017.01	1633.35	761.58	303.79
65.75	837.71	1394.89	600.09	244.04	779.28	1560.11	566.85	288.98
65.78	8828.48	1343.74	6228.12	244.09	9789.34	1498.46	6737.47	270.24
65.78	2637.91	1317.97	1730.26	230.46	3236.23	1466.79	1994.30	285.05
65.78	1096.04	1317.97	796.20	230.46	1706.03	1466.79	1105.05	285.05
65.8	647.72	1317.97	555.57	230.46	536.03	1466.79	468.11	285.05
65.82	1193.28	1378.99	1041.94	219.49	1179.13	1529.33	1030.68	345.31
65.823	734.17	1378.99	685.44	219.49	773.09	1529.33	720.03	345.31
65.839	890.15	1290.46	867.90	284.64	1164.42	1424.61	1129.01	407.48
65.88	2741.19	689.01	2987.63	464.19	2582.82	603.25	2803.32	491.62
65.91	765.26	1046.32	854.17	557.34	863.06	895.81	973.78	584.62
65.92	991.72	1085.46	1424.29	588.39	840.18	930.73	1150.85	620.59
65.96	4722.21	1329.72	6996.71	667.16	4147.27	1131.42	5915.92	675.02
65.98	1200.89	1484.94	2259.18	639.78	1283.03	1256.93	2510.40	700.88
66.06	754.36	142.18	1414.13	401.05	778.76	167.40	1489.07	356.65
66.09	695.33	94.68	1179.23	263.07	646.99	103.38	1062.53	233.94
66.1	712.46	90.27	1274.50	217.08	497.51	97.29	764.87	198.10
66.11	670.30	84.95	1177.58	205.44	569.78	91.13	930.55	199.55
66.12	566.36	81.86	946.76	193.81	534.14	87.60	872.12	192.12
66.14	735.46	142.64	1429.91	192.69	688.80	141.15	1287.21	182.07
66.15	776.21	174.63	1647.99	191.46	750.04	173.64	1552.00	179.37
66.16	794.60	193.17	1711.90	188.56	733.15	197.88	1487.66	178.39
66.16	782.20	193.17	1669.88	188.56	746.02	197.88	1537.17	178.39
66.163	797.89	193.17	1744.27	188.56	799.33	197.88	1750.00	178.39
66.17	915.36	209.16	2300.43	187.03	757.50	217.04	1603.70	176.66

66.177	899.14	227.07	2276.25	185.50	891.56	236.89	2236.49	177.10
66.188	792.46	245.52	1823.85	185.64	609.93	256.65	1162.70	179.80
66.19	652.29	245.52	1879.22	185.64	510.50	256.65	1162.57	179.80
66.22	2796.35	312.29	/	186.51	2666.13	327.12	/	207.61
66.22	1289.14	312.29	/	186.51	1007.11	327.12	36850.16	207.61
66.23	813.20	350.46	40938.28	186.46	921.57	365.88	/	220.33
66.237	1073.19	350.46	/	186.46	1815.04	365.88	/	220.33

*Model 1 uses SST data from Linnert et al. (2014) and $\delta^{13}C_{org}$ following Caves et al. (2016). $\delta^{13}C_{carb}$ is the only in-situ measurement

*Model 2 uses SST data from Linnert et al. (2014) with in-situ $\delta^{13}C_{org}$

*Model 3uses in-situ soil temperature with $\delta^{13}C_{org}$ following Caves et al. (2016).

*Model 4 uses in-situ soil temperature and $\delta^{13}C_{org}$